Characterization of Arctic ice cloud properties observed during ISDAC

Caroline Jouan, Eric Girard, Jacques Pelon, Ismail Gultepe, Julien Delanoë, Jean-Pierre Blanchet

Characterization of Arctic ice cloud properties observed during ISDAC

Caroline Jouan,[1,2] Eric Girard,[1] Jacques Pelon,[2] Ismail Gultepe,[3] Julien Delanoë,[4] and Jean-Pierre Blanchet[1]

Received 3 April 2012; revised 21 September 2012; accepted 16 October 2012; published 13 December 2012.

[1] Extensive measurements from ground-based sites and satellite remote sensing (CloudSat and CALIPSO) reveal the existence of two types of ice clouds (TICs) in the Arctic during the polar night and early spring. The first type (TIC-2A), being topped by a cover of nonprecipitating very small (radar unseen) ice crystals (TIC-1), is found more frequently in pristine environment, whereas the second type (TIC-2B), detected by both sensors, is associated preferentially with a high concentration of aerosols. To further investigate the microphysical properties of TIC-1/2A and TIC-2B, airborne in situ and satellite measurements of specific cases observed during Indirect and Semi-Direct Aerosol Campaign (ISDAC) have been analyzed. For the first time, Arctic TIC-1/2A and TIC-2B microstructures are compared using in situ cloud observations. Results show that the differences between them are confined in the upper part of the clouds where ice nucleation occurs. TIC-2B clouds are characterized by fewer (by more than 1 order of magnitude) and larger (by a factor of 2 to 3) ice crystals and a larger ice supersaturation (of 15–20%) compared to TIC-1/2A. Ice crystal growth in TIC-2B clouds seems explosive, whereas it seems more gradual in TIC-1/2A. It is hypothesized that these differences are linked to the number concentration and the chemical composition of aerosols. The ice crystal growth rate in very cold conditions impinges on the precipitation efficiency, dehydration and radiation balance. These results represent an essential and important first step to relate previous modeling, remote sensing and laboratory studies with TICs cloud in situ observations.

Citation: Jouan, C., E. Girard, J. Pelon, I. Gultepe, J. Delanoë, and J.-P. Blanchet (2012), Characterization of Arctic ice cloud properties observed during ISDAC, *J. Geophys. Res.*, *117*, D23207, doi:10.1029/2012JD017889.

1. Introduction

[2] According to the *Intergovernmental Panel on Climate Change* [2007] and *Hassol* [2005], the Arctic region is undergoing the most rapid and severe climate change on Earth. Since the 1960s, the Arctic mean annual surface air temperature has been increasing at about twice the global mean rate. The amplitude and future evolution of Arctic warming are highly uncertain. Cloud feedbacks have been recognized as the key source of uncertainty in climate sensitivity estimates using Global Climate Models (GCMs) [*Dufresne and Bony*, 2008]. Clouds play a fundamental role both (1) in modulating atmospheric radiation by altering the solar and infrared radiation at the surface and at the top of the atmosphere and (2) in modulating the hydrologic cycles by the conversion of water vapor to liquid and solid particles. This is particularly critical in the Arctic, where interactions can be enhanced by the presence of aerosols [*Grenier and Blanchet*, 2010; *Morrison et al.*, 2005]. *Shupe et al.* [2011] have shown that the annual cloud fraction derived from ground-based remote sensor measurements increases from 58 to 83% between winter and summer at six Arctic observatories over land or near land-ocean shore (Barrow, Atqasuk, SHEBA, Eureka, Ny'Alesund, Summit). The annual mean net radiative effect of these Arctic clouds is a warming for most of the year, except for a short period during the summer [*Intrieri et al.*, 2002]. The surface cloud forcing strongly depends on cloud properties (phase, optical depth, water content, particle size, temperature and height), solar zenith angle, and surface albedo [*Shupe and Intrieri*, 2004].

[3] Arctic cloud properties have been described in a number of observational studies using aircraft, ground-based remote sensors and satellites, especially related to the investigation of low-level mixed phase cloud properties.

[1]ESCER Centre, Department of Earth and Atmospheric Sciences, University of Quebec at Montreal, Montreal, Quebec, Canada.
[2]Laboratoire Atmosphère, Milieux et Observations Spatiales, Paris, France.
[3]Environment Canada, Toronto, Ontario, Canada.
[4]Laboratoire Atmosphère, Milieux et Observations Spatiales, Guyancourt, France.

Corresponding author: C. Jouan, ESCER Centre, Department of Earth and Atmospheric Sciences, University of Quebec at Montreal, 201 Ave. du Président-Kennedy, Montreal, QC H3C 3P8, Canada. (jouan.caroline6@gmail.com)

0148-0227/12/2012JD017889

However, *Shupe* [2011] has shown that ice-only clouds are more common than mixed phase clouds with similar longevity according to the annual average statistics for the western Arctic sites (Barrow, Eureka, SHEBA). Although some studies show that ice nuclei (IN), in the context of diamond dust [*Intrieri and Shupe*, 2004] and subvisible Arctic ice cloud properties [*Lampert et al.*, 2009], have a small effect on the radiation budget at the surface, their existence could be important in the Arctic spring to (1) maintain mixed phase low clouds [*Morrison et al.*, 2005, 2011] or (2) in winter when the warming resulting from the "cloud greenhouse effect (thermal)" is not balanced by the cooling resulting from the "cloud albedo forcing (solar)" [*Girard and Blanchet*, 2001; *Shupe and Intrieri*, 2004].

[4] The formation and evolution of ice in clouds are still poorly understood in part because of the complexity of ice particle nucleation processes. The processes by which ice forms and evolves in ice clouds were mostly investigated in midtropospheric and upper tropospheric ice clouds including wave and cirrus clouds [*Lawson et al.*, 2001; *Baker and Lawson*, 2006a; *Lawson et al.*, 2006b; *Sassen et al.*, 2001; *Heymsfield et al.*, 2002]. These studies suggest that ice particles in cirrus first go through a conversion from water vapor to liquid and solution droplets, which freeze at low temperatures to form polycrystalline ice particles by immersion and/or contact freezing (above $-38°C$) or homogeneous freezing (below $-37°C$) on deliquesced aerosols without the need for ice nuclei. However, the relative importance of each of the above mentioned processes to the ice crystal nucleation in these ice clouds is still highly uncertain.

[5] The joint detection characteristics of both the CloudSat radar and CALIPSO lidar recently reveal the existence of two Types of extended Ice Clouds (TICs) in the Arctic during the polar night and early spring [*Grenier et al.*, 2009; *Grenier and Blanchet*, 2010]. The type refers to the number of active instruments detecting the cloud; ice clouds of type 1 (TIC-1) are only seen by the lidar, whereas ice clouds of type 2 (TIC-2) are seen by both the lidar and the radar. TIC-2 is further divided into TIC-2A and TIC-2B. TIC-2A is topped by a substantial layer of very small (radar unseen) ice crystals (TIC-1). In contrast, TIC-2B is not overlaid by TIC-1. In this paper, TIC-1 and TIC-2A are not differentiated and therefore will be identified as TIC-1/2A. According to *Grenier et al.* [2009], TIC-1/2A and TIC-2B clouds form preferentially in pristine and polluted environment, respectively. Polluted air masses in the Arctic are associated with the long-range transport of anthropogenic pollution from the midlatitudes, primarily originating from Eurasia [*Law and Stohl*, 2007; *Hirdman et al.*, 2010], to the Arctic. Aerosol concentrations are the largest during winter and spring seasons by nearly 2 orders of magnitude (known as Arctic haze) as compared to summer due to favorable large-scale atmospheric circulation and few precipitations north of the polar front, thus limiting wet scavenging of aerosols [*Sirois and Barrie*, 1999]. The dominant component of these pollutant-enriched aerosols is highly acidic sulphate [*Barrie and Barrie*, 1990; *Quinn et al.*, 2007], which coats most of the aerosols of the accumulation mode during its long-range transport [*Bigg*, 1980]. It has been shown that acid coating on dust aerosols substantially increases the onset ice supersaturation for ice nucleation [*Eastwood et al.*, 2009; *Chernoff and Bertram*, 2010; *Sullivan et al.*, 2010]. *Blanchet and Girard* [1994] have hypothesized that the decrease of the IN concentration in polluted air masses results to a smaller concentration of larger ice crystals, leading to precipitation (i.e., cloud regime TIC-2B), because of the reduced competition for the same available moisture. Therefore, the ice crystal precipitation rate and the rate of dehydration of the lower troposphere increase while the water vapor and TIC-2B greenhouse effect decreases at the expense of nonprecipitating ice clouds (TIC-1). At cold Arctic winter temperature, the greenhouse effect in the so-called dirty window (17 to 35 μm) is especially sensitive to atmospheric dehydration. Positive feedback is created between the midtroposphere and lower troposphere cooling and dehydration efficiency, increasing the production rate of cold and dry air masses. This process is referred to as the Dehydration Greenhouse Feedback (DGF) [*Blanchet and Girard*, 1994].

[6] This research aims to characterize the microphysical properties of TIC-1/2A and TIC-2B clouds using airborne in situ and satellite measurements. The observational data set is from the Department of Energy (DOE) Atmospheric Radiation Measurement (ARM) Indirect and Semi-Direct Aerosol Campaign (ISDAC) [*McFarquhar et al.*, 2011], which was conducted over the North Slope of Alaska (NSA), during April 2008. One of the main objectives of ISDAC project was to examine the influence of the arctic aerosol on cloud microphysical properties and on the surface energy balance. During ISDAC, the National Research Council of Canada (NRC) Convair-580 was equipped with 41 instruments including a complete set of dynamic, thermodynamic, radiation, aerosol and microphysical sensors. Twenty-seven scientific flights were performed under various weather conditions. Flight profiles consisted of spiral and ramped ascents and descents through clouds and constant altitude legs within and outside clouds between Barrow and Fairbanks. The strategy was also to coordinate flights with other aircrafts (NASA DC8, P-3B, B200, NOAA WP-3D) and satellite overpasses (A-Train).

[7] For the first time, Arctic TIC-1/2A and TIC-2B clouds are characterized using in situ observations. Although the data set used in this study is rather limited, results of the cases studied in this paper provide the first detailed in situ measurements of Arctic TICs and highlight the microstructure differences between TIC-1/2A and TIC-2B. These results represent an essential and important first step to relate previous modeling, remote sensing and laboratory studies mentioned above with TICs cloud in situ observations.

[8] This paper is organized as follow. In section 2, ISDAC ice clouds are identified and airborne instruments used for the measurements are described. Section 3 presents the variability in number concentration of ice particles, ice water content and ice particles effective radius as a function of ice supersaturation and air temperature of all ice clouds investigated in this study. A detailed study on the microphysical and thermodynamical properties of two case studies of ice clouds is also carried out in section 3. A discussion and conclusions are presented in sections 4 and 5, respectively.

2. Observations and Methodology

2.1. Identification of Ice Clouds

[9] The greatest challenge in the study of ice clouds observed during ISDAC is the discrimination of ice clouds

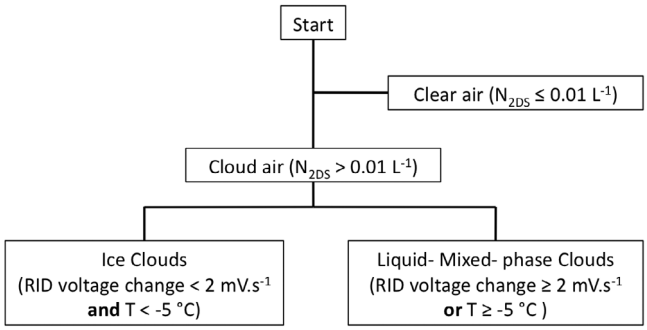

Figure 1. Algorithm used to identify the phase (ice, liquid or mixed phase cloud) of each 30 s period of in situ data.

from the mixed phase clouds. Liquid water content (LWC) probes can strongly respond to ice particles too [*King et al.*, 1978; *Cober et al.*, 2001; *Gultepe et al.*, 2001]. To circumvent this problem, the Rosemount Icing Detector (RID) sensor was used to detect the presence of supercooled liquid water in ice and mixed phase clouds. The RID probe measures the rate of voltage change (dV_R/dt mV s^{-1}) converted from the decrease of the vibration's frequency of the cylinder due to the accumulation of ice on its surface. When the cylinder oscillation frequency reaches a minimum threshold value, the cylinder is heated to melt the ice [*Mazin et al.*, 2001; *Cober et al.*, 2001]. According to *Cober et al.* [2001], the sensitivity threshold of the RID signal for the presence of supercooled liquid water is 2 mV s^{-1} with higher values in conditions with air temperature (T_a) below −5°C [*Mazin et al.*, 2001; *Gultepe et al.*, 2001]. To detect the presence of ice particles, we used the optical array probe 2DS covering the largest spectrum of particles with diameters ranging between 10 and 1280 μm. Because of a common lower limit for instruments in measuring low concentrations of small ice crystals, ice clouds with an ice crystal number concentration (N_{ic}) smaller than 0.01 L^{-1} are not taken into account. Therefore, in our study, clouds with $T_a < -5$°C, $N_{ic} > 0.01$ L^{-1} and $dV_R/dt < 2$ mVs^{-1} were considered as ice clouds. Figure 1 shows the algorithm used to identify the thermodynamic phase (ice, liquid or mixed) of the investigated clouds. This analysis is performed using 30 s averaged values of T_a, N_{ic} and dV_R/dt. This algorithm was applied for all ISDAC data and used to select ice clouds investigated in this study. Ice clouds with temperature warmer than -30 ± 0.5°C are not included in the analysis. Table 1 shows the time interval of all selected ice cloud profiles. Ice clouds may contain a trace amount of liquid water are identified in Table 1. They are defined as clouds in which some instantaneous (1 s) RID values within a 30 s average are larger than 2 mV s^{-1}. One instantaneous (1 s) RID value larger than 2 mV s^{-1} can also be considered as noise. The 30 s averaged RID value remains however below this threshold.

2.2. Airborne Thermodynamical, Microphysical and Aerosol Instruments

[10] Instruments used to measure cloud thermodynamic properties were the Rosemount 102 and the reverse flow temperature probes for the air temperature; and the EG&G chilled mirror for the relative humidity with respect to liquid water and ice [*Gultepe and Starr*, 1995]. The EG&G hygrometer uses a chilled mirror to determine dew or frost point. The dry and clean mirror is monitored by an optical sensor and is cooled until the moisture condenses on it. The optical sensor detects changes in the reflective properties of the mirror caused by moisture and sends a signal to the cooling system to reduce the current and allow the mirror to warm up. This cycle continues until a layer of constant moisture thickness is formed on the mirror surface. The temperature at which this stability is reached is the dew point (above 0°C) or the frost point (below 0°C) if within the ice clouds. For all ice clouds defined in Table 1, temperature differences between both temperature sensors indicate that the averaged uncertainty is about ±0.5°C. Air temperature measurements from the reverse-flow temperature probe were used in this study. The uncertainty of the derived relative humidity ranges from 4.7% to 10.9% at cold temperatures [*Lin and Hubbard*, 2004].

[11] The main parameters to describe the cloud microphysical and optical properties are the cloud particle size distribution (PSD) and the bulk quantities (total number concentration of ice crystals (N_{ic}), extinction coefficient (β_{ext}), ice water content (IWC) and ice crystal effective radius (R_{ei})). Available instruments to measure individual cloud particles were the FSSP-100 (3–45 μm), 2 DC (25–800 μm) and 2DP (200–6400 μm) developed by Particle Measuring Systems (PMS); the CDP (2–50 μm), CAS (1–50 μm) and CIP (15–1550 μm) developed by Droplet Measurement

Table 1. Time and Spatial Coordinates of the Ice Cloud Profiles Selected by the Algorithm of Figure 1 for Which the Cloud Temperature Drops Below $-30° \pm 0.5$°C During the ISDAC Measurement Campaign

Date (yy/mm/dd)	Flight	Place	Flight Type	ΔT Ice Cloud (IC) (hh:mm:ss)		IC May Contain H_2O_{liq}	MP Cloud in Lower Layers	Code
08/04/01	F9	Barrow	Descent Spiral	23:14:00	23:31:30	No	Yes	F9
08/04/04	F11	Barrow	Descent Spiral	19:33:30	19:51:00	No	Yes	F11
08/04/05	F12	Barrow	Ascent Spiral	01:21:00	01:33:30	No	No	F12
08/04/05	F13	Fairbanks	Ascent Ramped	17:40:30	17:59:30	Yes	Yes	$F13_1$
08/04/05	F13	Barrow	Descent Spiral	19:18:00	19:37:30	Yes	Yes	$F13_2$
08/04/05	F13	Barrow	Descent Spiral	20:35:30	20:55:00	Yes	Yes	$F13_3$
08/04/05	F14	Barrow	Descent Spiral	23:07:00	23:23:00	Yes	Yes	F14
08/04/08	F15	Fairbanks	Ascent Ramped	15:00:30	15:16:00	No	No	F15
08/04/14	F20	Barrow	Descent Spiral	19:51:30	20:14:00	Yes	No	F20
08/04/15	F21	Barrow	Ascent Spiral	00:55:30	01:16:00	Yes	No	F21
08/04/19	F24	Barrow	Ascent Ramped	01:23:30	01:41:30	Yes	Yes	F24
08/04/25	F29	Barrow	Ascent Ramped	02:27:00	02:38:30	No	No	F29

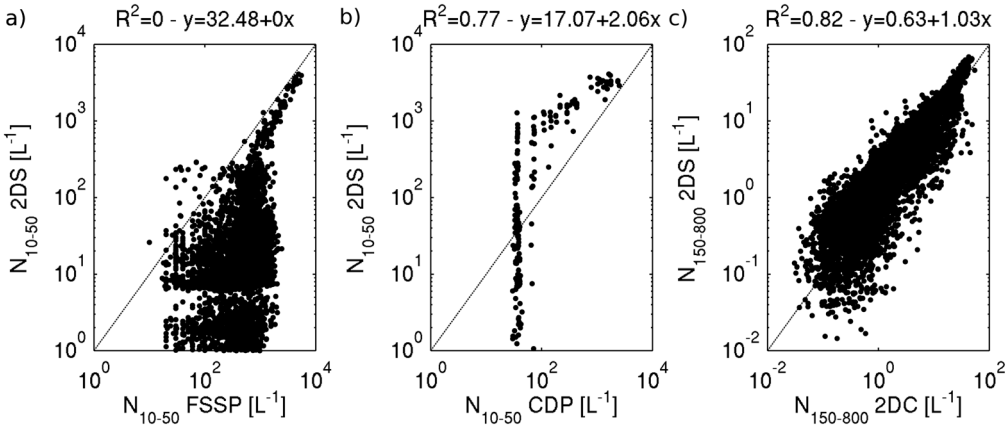

Figure 2. (a) FSSP concentration as function of 2DS concentration (10–50 μm). (b) CDP concentration as function of 2DS concentration (10–50 μm) for ice clouds defined in Table 1 with $T_a < -15$°C. (c) The 2DC concentration as function of 2DS concentration (150–800 μm) for ice clouds defined in Table 1.

Technologies (DMT); and the 2DS (10–1280 μm) and CPI (15–2500 μm) developed by Stratton Park Engineering Company (SPEC). These instruments measure the number concentration and size distribution of ice crystals. The bulk quantities are derived from the measured size distribution as described in section 2.4. The NRC Convair-580 was also equipped with a CPI probe to record images of particles on a charge-coupled device (CCD) image sensor in a digital camera, that passes through the intersection of the two laser beams [*Lawson et al.*, 2001].

[12] Previous studies investigating the performance of cloud probes in ice conditions suggest that shattering of large ice crystals on the inlets and tips has a strong impact on the CAS cloud particle size distribution measurements compared to the CDP, CPI and 2DS [*McFarquhar et al.*, 2007; *Jensen et al.*, 2009; *Protat et al.*, 2011] and on the FSSP cloud particle size distribution measurements compared to the CDP and 2DS probes [*McFarquhar et al.*, 2011]. The impact of shattering is likely to be small for the CDP probes [*McFarquhar et al.*, 2007; *Protat et al.*, 2011; *Lance et al.*, 2010; *McFarquhar et al.*, 2011]. Shattering artifacts can also occur in all of the Optical Array Probes (OAPs) as a result of large crystals hitting the detector arms [*Field et al.*, 2006]. Techniques currently used to reduce the effects of shattering include the use of redesigned probe tips and algorithms to eliminate closely spaced particles, which are assumed to result from shattering. The effectiveness of a technique rather than the other is still being evaluated [*Korolev et al.*, 2011; *Lawson*, 2011]. Shattered artifacts have been removed from the 2DS, 2DC and 2DP data using algorithms to eliminate closely spaced particles of sizes smaller than 50 μm (the 2D-S arrival time algorithm was developed and applied by Paul Lawson's group at Stratton Park Engineering Company [*Lawson*, 2011, Appendix B] and the 2D-C and 2D-P arrival time algorithm was developed and applied by G. McFarquhar's group at the University of Illinois). However, *Korolev et al.* [1998] and *Lawson et al.* [2006a] have shown that particles smaller than approximately 100 μm in diameter collected by the 2DC have counting and sizing errors. For these reasons, data from the FSSP and CAS probes and cloud particle size distributions from the 2DC probe for diameters smaller than 150 μm are not used in this study. It is important to note that every instrument used to measure individual cloud particles can be subject to shattering signatures and/or other sources of contamination and limitations specific to the probe. Therefore a combination of instruments is needed to detect a wide range of cloud particle population. The aerosol number concentration (N_a) was measured with the CPC-3775 (>0.004 μm) developed by Trust Science Innovation (TSI) and the PCASP (0.12–3 μm) developed by PMS. Note that data from the CPC-3775 were good for lower altitudes only ($\sim$<3.5 km above mean sea level) due to instrument limitation. Data from the PCASP were missing for flights F20 and F21. A single mass spectrometer (SPLAT II) measuring the concentration and chemical composition of aerosols [*Zelenyuk et al.*, 2010] and a continuous flow diffusion chamber (CFDC) measuring the IN concentration were also available in the aircraft. Unfortunately, the CFDC was not functional for flights prior to 8 April 2008 (including Flight 8-15). SPLAT II has allowed characterization of the background, activated and interstitial particles with their chemical composition in a mixed phase stratocumulus sampled on 26 April 2008 during ISDAC [*Zelenyuk et al.*, 2010]. Information that can provide this instrument could be crucial in our study, however, since the concentration of ice crystals in ice clouds is typically 2 to 4 orders of magnitude lower than that of droplets in warm clouds, the characterization of IN, in field measurements, is drastically more difficult than the characterization of CCN. Then aerosol chemical composition from SPLAT II for F9 and F21 were not available at the beginning of the analysis (A. Zelenyuk, personal communication, 2011).

2.3. Performance of Instruments Measuring Individual Cloud Particles

[13] In this section, statistical comparisons are made to evaluate the performance of ice crystal measurements and derived products from the FSSP, CDP, 2DS and 2DC during ISDAC. Figure 2 shows a comparison between the FSSP ($N_{ic:10–50,FSSP}$), CDP ($N_{ic:10–50,CDP}$) and 2DS ($N_{ic:10–50,2DS}$) ice crystal number concentrations for diameters ranging from 10 to 50 μm, at air temperature below -15°C, and the 2 DC ($N_{ic:150–800,2DC}$) and 2DS ($N_{ic:150–800,2DS}$) ice crystal

number concentrations for diameters ranging from 150 to 800 μm, during all ice clouds considered in this study (see Table 1). We found no correlation between $N_{ic:10–50,FSSP}$ and $N_{ic:10–50,2DS}$ (Figure 2a) and a correlation of $R^2 = 0.77$ between $N_{ic:10–50,CDP}$ and $N_{ic:10–50,2DS}$ (Figure 2b). Nevertheless, only 25.7% of the data points were nonzero for the CDP data against 72.5% for the 2DS data in this size range. On the other hand, a better correlation ($R^2 = 0.82$) is obtained between $N_{ic:150–800,2DS}$ and $N_{ic:150–800,2DC}$ for all ice clouds (Figure 2c). Using the CDP to measure ice crystal PSDs has not been well established for ice clouds. It is very difficult to give a definitive answer as to whether it is better to use a 2DS or CDP in the size range between 10 and 50 μm because 2DS measurements may be affected by particle shattering in that size range. There are a lot of uncertainties in the measurement of small ice crystals. That is why it is generally suggested to use different measurements to give a better idea of the upper and lower bounds of the concentrations in various different size ranges (G. McFarquhar, personal communication, 2011). However, in this study, the 2DS is preferred for diameters ranging from 10 to 50 μm since the CDP probe was calibrated for liquid water during ISDAC. During ISDAC, 2DS was also the only instrument that can measure ice crystals with diameters ranging from 50 to 150 μm, a size range that has been traditionally difficult to measure. Therefore, the two combinations of the PSDs used in this study were the following: (1) 2DS for $N_{ic}(10 < D < 150\ \mu m)$, 2 DC for $N_{ic}(150 < D < 800\ \mu m)$, 2DP for $N_{ic}(D > 800\ \mu m)$ and (2) 2DS for $N_{ic}(10 < D < 800\ \mu m)$, 2DP for $N_{ic}(D > 800\ \mu m)$.

2.4. Derived Bulk Parameters

[14] This section describes how the ice cloud bulk properties were determined from the 2DS and 2DC-P probes data. The total number of ice particle (N_{ic}) from the three instruments was directly estimated from the size spectrum as a function of the particle diameter, $N_i(D_i)$.

[15] Using the 2DS probes data, the crystal mass (m_i in mg) was estimated either from the ice crystal projected area (A_i in mm^2) using the equation of *Baker and Lawson* [2006b] (here after referred to as BL06):

$$m_i = 0.155 A_i^{1.218} \tag{1}$$

or from the equivalent volume of a sphere with diameter (D_i) of the ith size bin. The smaller estimate is used. The projected area is based on the area that is directly measured by the 2DS probe. Area and mass are summed to yield time series of extinction coefficient and ice water content, respectively. Assuming that particles are larger than the incoming radiation, a factor 2 is applied for the extinction coefficient calculation using Mie theory.

[16] Using the 2DC and 2DP probes data, the crystal mass in each size interval is also estimated as a function of the crystal maximum diameter (D_i in mm) using

$$m_i = \alpha D_i^{\beta} \tag{2}$$

where α and β are habit-dependent coefficients [*Heymsfield et al.*, 2002]. We used $\alpha = 0.021$ and $\beta = 2.0$ following *Mitchell et al.* [1990] (hereafter referred to as M90).

[17] The uncertainties in the bulk measurements are mainly due to uncertainties on the recognition of the type of particle in the choice of mass-diameter relationship. The data set used to define both BL06 and M90 relationships was obtained by collecting ice particles falling from winter storms in the Sierra Nevada of California in 1987 [*Mitchell et al.*, 1990]. Coefficients used in equations (1) and (2) represent all ice particles types (all shapes included) sampled in the M90 data set. We assumed that the M90 and BL06 assumptions hold for the similar temperature and relative humidity seen during ISDAC. However, we must keep in mind that certain types of particles in our study wouldn't actually match a decent fraction of those included in the data set of *Mitchell et al.* [1990]. For example, crystal type such as bullet rosette is not represented in the M90 data set, while one of the two ice clouds studied in detail in section 3.3 is mainly composed of this crystal type. The special software to perform habit classification and calculation of the area, volume, and other characteristics of the particles could not be used since it is not available by other scientists. Thus systematic errors can be introduced on a flight segment (in which the particle shape does not correspond with the selected D-mass relationships) and thus be particularly significant in the derived bulk measurements.

[18] The ice water content is then obtained using

$$\mathrm{IWC} = \sum_{i=1}^{n} m_i N_i(D_i) \Delta D_i \tag{3}$$

where ΔD_i is the width of the ith size bin and n is the number of size bins. Since the projected area is unknown, the equivalent diameter (D_{eq}) is calculated to obtain the extinction coefficient. D_{eq} is the diameter of an equivalent sphere having the same mass as an ice crystal mass of a given size bin (m_i) and is given by

$$D_{i,eq} = (6 m_i / \pi \rho_{ice})^{1/3} \tag{4}$$

where ρ_{ice} is the bulk density of ice, which was assumed to be equal to 0.91 g cm^{-3}.

[19] The extinction coefficient is proportional to the second power of particles size and is given by

$$\beta_{ext} = \sum_{i=1}^{n} 2 D_{i,eq}^2 N_i(D_i) \Delta D_i \tag{5}$$

The ice crystal effective radius (R_{ei}) is obtained by dividing the third and second powers of the ice crystal size distribution as follows:

$$R_{et} = 1/2 \left(\sum_{i=1}^{n} D_{i,eq}^3 N_i(D_i) \Delta D_i \Big/ \sum_{i=1}^{n} D_{i,eq}^2 N_i(D_i) \Delta D_i \right) \tag{6}$$

where $D_{i,eq}$ is for equivalent diameter of ice spheres having the same volume. $N_i(D_i)$ is either obtained from the integration of 2DS, 2DC, and 2DP data or from the integration of 2DS and 2DP probes data (equations (2) and (4)).

[20] Figure 3 shows a comparison of the ice water content (Figures 3a and 3b), the extinction coefficient (Figures 3c and 3d) and the effective radius (Figures 3e and 3f) obtained from the two combinations of the PSDs defined

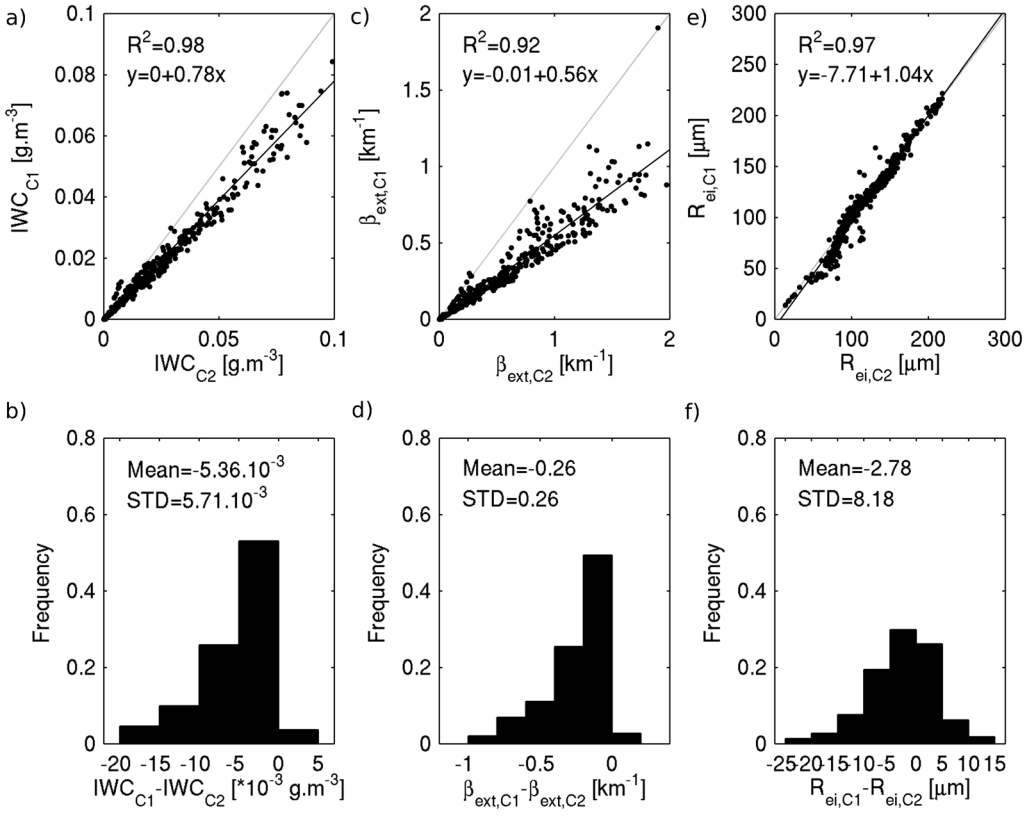

Figure 3. Comparison of (a, b) IWC, (c, d) β_{ext} and (e, f) R_{ei} from combinations (1) 2DS for $N_{[10<D<150\mu m]}$, 2 DC for $N_{[150<D<800\mu m]}$, 2DP for $N_{[D>800\mu m]}$ and (2) 2DS for $N_{[10<D<800\mu m]}$, 2DP for $N_{[D>800\mu m]}$ for ice clouds defined in Table 1.

previously on the set of points of ice clouds defined in Table 1. Data are averaged over 30 s periods. We found very good correlation ($R^2 \geq 0.92$) between both PSD combinations, i.e., between the 2DS and 2DC probe data for diameters ranging from 150 to 800 μm. The 2DS and 2DC concentration and IWC differ by a factor 1.4. As a result, the 2DS extinction coefficient should be about 1.4 times larger when compared to the 2DC extinction coefficient. A factor of 2 is obtained between both extinction coefficients, implying that the 2DS's area per particle is a bit too large. This means that the 2DS instrument does not agree within experimental uncertainty with respect to the values of the extinction coefficient but there is an overestimation of the retrieved 2DS's area per particle. Differences of the ice water content, the extinction coefficient and the ice effective radius do not exceed ± 0.02 g m^{-3}, ± 1.0 km^{-1} and ± 25 μm respectively with a standard deviation of 0.057 g m^{-3}, 0.26 km^{-1} and 8.18 μm (Figures 3b, 3d, and 3f). The distribution of IWC, β_{ext} and R_{ei} differences suggests that the average random error in the bulk measurements can be estimated as approximately ± 0.01 g m^{-3} for IWC, ± 0.5 km^{-1} for β_{ext} and ± 15 μm for R_{ei} (frequency >80%) for diameters ranging from 150 to 800 μm. For particles smaller than 150 μm or larger than 800 μm, both combinations 1 and 2 in the Figure 3 caption use the same instrument. Therefore, one cannot estimate a random error from the difference between both combinations for these sizes. Nevertheless, it was assumed that the uncertainties on the PMS measurements of the concentration of ice crystals, the particle size, the extinction coefficient and the ice water content are respectively: 50%, 25%, 60% and 75% [*Gayet et al.*, 2002]. These uncertainties will be accounted for in the interpretation of the results.

[21] Other "bulk microphysical measurements" such as the Nevzorov (TWC, LWC), King (LWC) and CSI (TWC) probes were not used either because they were not available at the beginning of the analysis or missing for some flights.

2.5. Remote Sensing Data

[22] ISDAC flight missions were coordinated with CloudSat and CALIPSO satellite overpasses. Satellite measurements provide useful information to identify cloud particle size and phase. They are valuable also in extrapolating some of the campaign's results to the broader Arctic region. Due to their respective wavelengths, radar and lidar are not sensitive to the same hydrometeore sizes. The lidar, with a relatively short wavelength, can detect small particles (aerosols, liquid drops, ice crystals) while the radar is more sensitive to larger particles (>$\sim$30 μm). However, the lidar signal becomes strongly attenuated when the optical depth approaches $\sim$3 (this value can vary depending on instrument specifications) [*Sassen and Cho*, 1992]. As a result, the lidar will not detect optically thin clouds if an optically thick cloud obstructs the lidar beam but radar measurement can penetrate more deeply ice clouds when lidar signal is extinguished.

[23] In this study, we use the variational synergistic algorithm (Varcloud) that was developed by *Delanoë and Hogan* [2008]. This algorithm combines both radar and lidar

observations to retrieve IWC, extinction and effective radius in regions of the cloud detected by just one of these two instruments. The ice particle mass is assumed to follow the *Brown and Francis* [1995] mass-D relationship and R_e is derived using [*Foot*, 1988]

$$R_e = (3\mathrm{IWC})/(2\rho_{\mathrm{ice}}\beta_{\mathrm{ext}}) \quad (7)$$

These operational products are called DARDAR and are available at the French data center ICARE in France. Retrieved properties are given at the CloudSat horizontal resolution (about 1.4 km) and 60 m vertical resolution. Details of the method are given by *Delanoë and Hogan* [2008, 2010]. The RMS error in ln IWC, ln β_{ext} and ln R_e (approximately equivalent to the fractional error in IWC, β_{ext} and R_e, respectively) are available in DARDAR products and derived according to the methodology of *Delanoë and Hogan* [2008]. These errors are associated with each measurement in the DARDAR database. Within the both TICs described and discussed in section 3.3, values of the RMS error in ln IWC, ln β_{ext} and ln R_e from DARDAR product ranging from 10 to 30% for IWC, from 20 to 40% for β_{ext} and less than 20% for R_e.

[24] *Delanoë et al.* [2012] have demonstrated the capability of DARDAR to retrieve cloud properties for an ice Nimbostratus cloud observed on 1 April 2008 during the POLARCAT (Polar Study using Aircraft, Remote Sensing, Surface Measurements and Models, of Climate, Chemistry, Aerosols, and Transport) campaign. They have shown that the synergetic combination of radar and lidar allows a better retrieval than the stand-alone retrievals when compared to the in situ measurements. DARDAR (radar/lidar) can be used most effectively for optically thin clouds due to lidar attenuation. Unfortunately, in situ measurements cannot be used as a qualitative evaluation of the satellites products since the colocation and the large inhomogeneities in the cloud can be sources of important errors. But they can give us a very good estimate of the order of magnitude for IWC, β_{ext} and R_{ei} retrievals.

3. Results

3.1. Selected Ice Clouds

[25] The following two criteria were considered to select ice cloud samples in our study. First, in situ measurements must fully cover the vertical extent of a given ice cloud including cloud top where ice nucleation is most likely to occur. The MicroPulse Lidar (MPL) [*Campbell et al.*, 2002] and the Millimeter Cloud Radar (MMCR) [*Moran et al.*, 1998] based at Barrow were used for flights made nearby to ensure that in situ measurements were performed from cloud top to cloud base. For flights nearby Fairbanks, this verification was made using the CALIOP lidar on board the CALIPSO satellite, closest in time and space from the airborne measurements. Flights for which the cloud top height could not be verified were rejected from the analysis. The second criterion is to select ice clouds with similar ice water content to avoid comparing clouds having too different ice mixing ratios. Ice clouds are rejected if the ice water content deviates by ±100% of the mean ice water content of the selected ice clouds (i.e., $\mathrm{IWC_{mean}} \sim 0.01 \pm 0.01$ g m^{-3} for $\mathrm{RH_{Ice}} > 100\%$).

[26] Figure 4a shows the ice water content (IWC) derived from the combination 2 (2DS + 2DP) as a function of relative humidity over ice ($\mathrm{HR_{Ice}}$). Each point on Figure 4a represents the averaged value of the ice water content within a 2% $\mathrm{RH_{Ice}}$ interval for all of the selected ice clouds profiles satisfying our first criterion (see Table 1). This study is focused on the area of the ice nucleation, therefore the set of points where $\mathrm{RH_{Ice}}$ is less than 100% in Figure 4 are not shown. Measurements derived from the combination 1 (2DS + 2DC + 2DP) (not shown) give similar results. Figure 4a shows that $\mathrm{F13_2}$, $\mathrm{F13_3}$, F14 and F24 do not satisfy the second criterion with IWC values larger by a factor of 4 to 8 compared to the averaged IWC value observed in the 7 other ice clouds at high relative humidity with respect to ice. They were therefore rejected from our analysis.

[27] Seven ice clouds (F9, F11, F12, F15, F20, F21 and F29) satisfying both selection criteria were selected for the analysis. One can distinguish two groups of ice clouds: the first one (F9, F11, F12 and F29) with a large concentration (exceeding 10 L^{-1}) of small ice crystals (smaller than 110 μm) and a second group (F15, F20 and F21) with a relatively small concentration (below 10 L^{-1}) of large ice crystals (larger than 110 μm). Table 2 shows the average ice crystal number concentration, the ice crystal effective radius and the aerosol concentration for the selected ice clouds. These two different groups of ice clouds in terms of ice crystal number concentration and effective radius suggest that the first and second group of ice clouds are representative of the TIC-1/2A and TIC-2B discussed above. The aerosol concentration observed in clear air just before entering the clouds show that these air masses were relatively clean with concentrations around or below 100 cm^{-3} with the exception of the flight F12 with larger concentrations. It should be noted that there were no PCASP measurements during flights F20 and F21 and no available measurements in clear air close enough to the cloud during flight F15.

3.2. N_{ic}-R_{ei} Versus RH_{Ice}-T_a Measurements: A Statistical Approach

[28] Figure 4b shows the number concentration of ice particles (N_{ic}) derived from the combination 2 as a function of the relative humidity with respect to ice ($\mathrm{HR_{Ice}}$). For the first type of ice clouds (TIC-1/2A) (F9, F11, F12 and F29 in gray full lines), N_{ic} tends to increase with increasing $\mathrm{RH_{Ice}}$ in flights F9 and F12 while no clear variation of N_{ic} with $\mathrm{RH_{Ice}}$ is obtained in F11 and F29. In the second type of ice clouds (TIC-2B) (F15, F20 and F21 in black full lines), N_{ic} is mostly independent of $\mathrm{RH_{Ice}}$. N_{ic} is systematically larger by more than 1 order of magnitude in TIC-1/2A when compared to TIC-2B for all $\mathrm{RH_{Ice}}$ values.

[29] Figure 4c shows the variation of R_{ei} as a function of $\mathrm{RH_{Ice}}$. TIC-2B R_{ei} is larger by a factor of 2 to 3 for all $\mathrm{RH_{Ice}}$ when compared to TIC-1/2A R_{ei}. While there is a clear tendency for R_{ei} to decrease with increasing $\mathrm{RH_{Ice}}$ for all ice clouds, R_{ei} decreases more rapidly with $\mathrm{RH_{Ice}}$ in TIC-1/2A when compared to TIC-2B R_{ei}, which never reaches values below 110 μm.

[30] Figure 4d shows the average relative humidity with respect to ice ($\mathrm{RH_{Ice}}$) as a function of air temperature (T_a) measured in all selected ice clouds profiles. According to *Korolev and Isaac* [2006], the relative humidity over ice tends to increase when the air temperature decreases with a

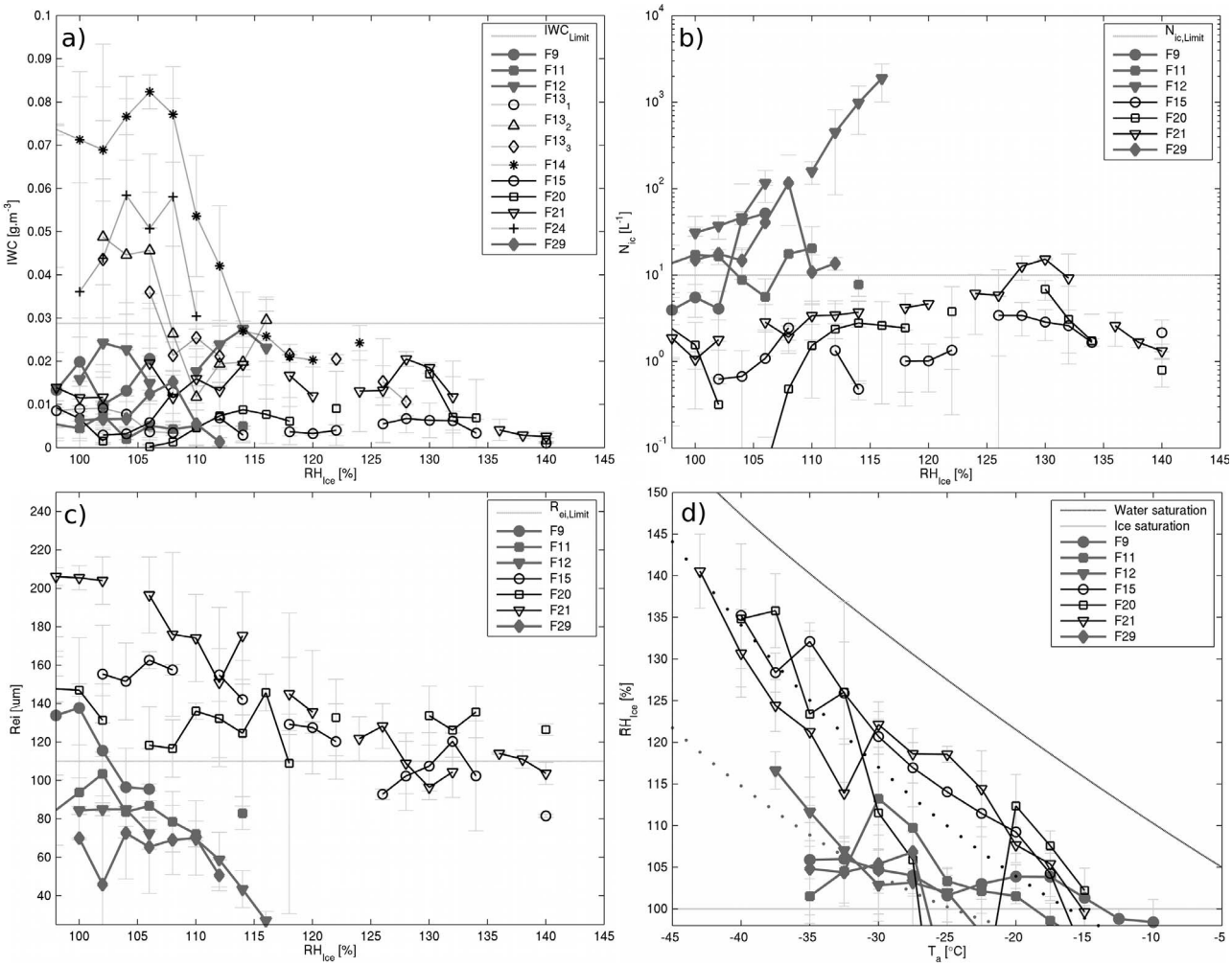

Figure 4. (a) IWC, (b) N_{ic} and (c) R_{ei} as function of RH_{Ice} averaged over 2% intervals and (d) RH_{Ice} as function of T_a averaged over 2.5°C intervals; vertical lines represent the standard deviations.

behavior that may be related to the type of ice cloud. In agreement with studies of *Korolev and Isaac* [2006] and *Korolev and Mazin* [2003], RH_{Ice} increases with the decrease of air temperature. RH_{Ice} values are generally between the ice and liquid saturation points. The interesting finding is that the behavior of the increase in RH_{Ice} with decreasing T_a appears to follow two patterns at colder temperature and $RH_{Ice} > 100\%$ depending on the type of the ice cloud. In TIC-1/2A (F9, F11, F12 and F29), which are composed by a large concentration of small ice crystals, RH_{Ice} never exceeds 120% (gray backslash). In TIC-2B (F15, F20 and F21), which are composed of a low concentration of relatively large ice crystals, RH_{Ice} is often larger than 120% (black backslash) at relatively cold temperature. The ice supersaturation in TIC-2B is 15% to 20% larger than in TIC-1/2A depending on the air temperature.

[31] High ice supersaturation has also been observed in previous campaigns [*Krämer et al.*, 2009, and references

Table 2. Flight Code, Cloud Top Height and Mean N_{ic} and R_{ei} for $RH_{Ice} > 100\%$ of Ice Clouds of Similar IWC (i.e., <0.03 g m^{-3})

Flight Code	Z_t: Ice Cloud Top Height[a] (m)	$N_{ic,mean}$	$R_{ei,mean}$	$N_{ic,mean} > 10\ L^{-1}$ $R_{ei,mean} < 110\ \mu m$	$N_{ic,mean} < 10\ L^{-1}$ $R_{ei,mean} > 110\ \mu m$	N_a[b] (cm^{-3})
F9	6646.5	26.12 ± 24.87[c]	111.32 ± 19.89	x		99.77 ± 14.92
F11	6648.5	13.41 ± 5.83	85.86 ± 10.23	x		44.82 ± 9.90
F12	7027.4	463.64 ± 660.85	65.65 ± 21.37	x		206.50 ± 127.02
F15	6690.9	1.75 ± 1.00	127.19 ± 26.10		x	-
F20	6502.6	2.18 ± 1.75	129.68 ± 10.56		x	-
F21	6748.5	4.92 ± 3.94	141.43 ± 38.29		x	-
F29	7057.8	32.66 ± 38.12	63.36 ± 10.63	x		105 ± 29.79

[a]Ice cloud top height from 30 s period airborne data.
[b]Aerosol concentration observed in clear air just before entering the cloud (1 min period averaged).
[c]Standard deviation of the points of Figure 3.

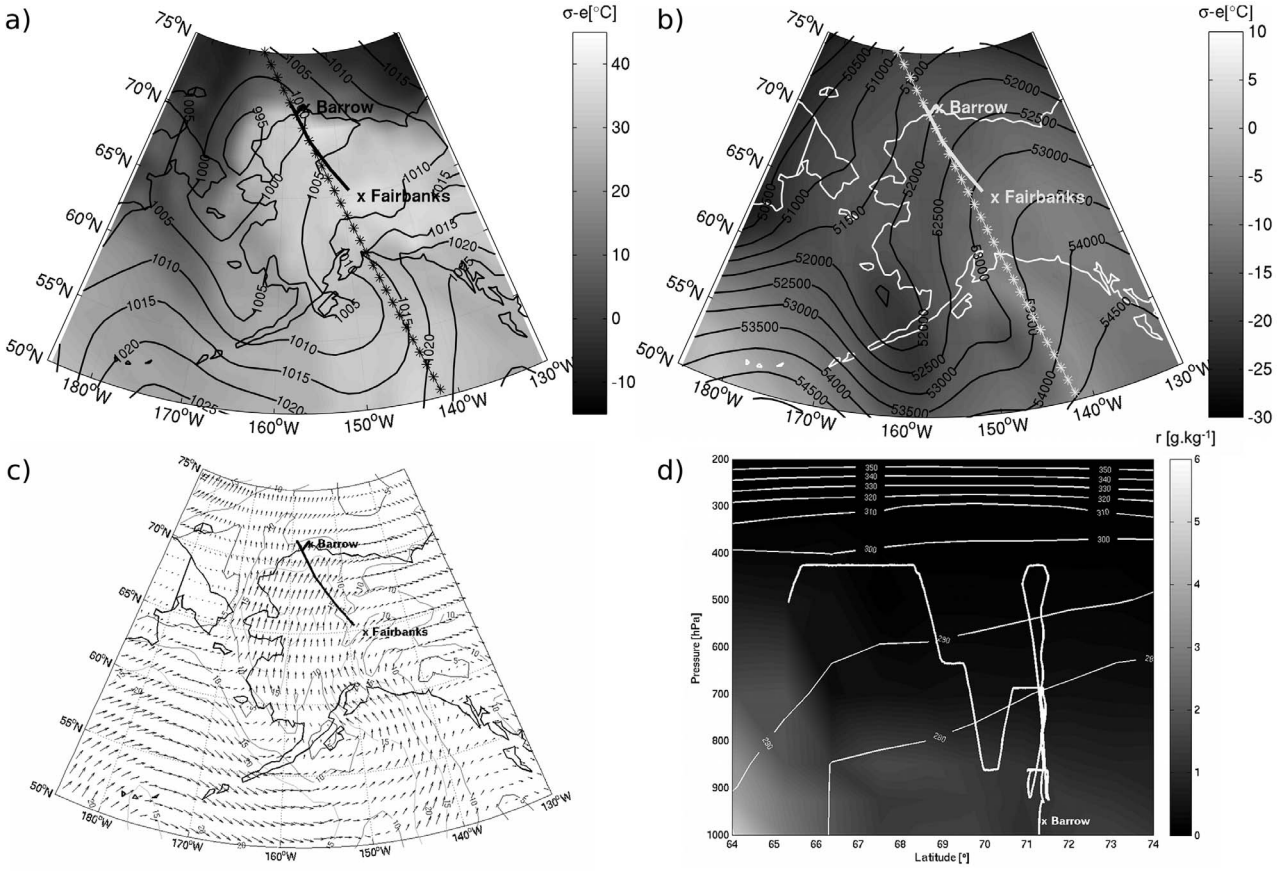

Figure 5. (a) Equivalent potential temperature (°C) with mean sea level pressure (hPa) and (b) geopotential (m^2 s^{-2}) at 500 hPa; (c) module and direction of horizontal wind at 700 hPa and (d) vertical profile of flight F9 (white solid line) with equivalent potential temperature (K) and mixing ratio (g kg^{-1}) over Alaska at 00:00:00 UTC, the 2 April 2008). A-Train overpass track (star line) is also shown at 22:37:14 UTC (1 April 2008).

therein]. *Krämer et al.* [2009] have reported high RH_{Ice} in tropical cirrus clouds at very cold temperatures. They also reported a smaller N_{ic} and larger R_{ei} for these clouds. However, in-cloud temperatures (−90°C to −40°C) were colder than the temperatures of our selected ice clouds (mostly above −40°C). It is therefore difficult to compare with our high RH_{Ice} selected clouds since the ice nucleation processes are likely to be different. For few warmer cases (−43 to −33°C), *Krämer et al.* [2009] reported RH_{Ice} varying between 100 and 120%, which is similar to the 4 TIC1/2A investigated in this paper. *Lawson et al.* [2008] have also reported high RH_{Ice} at very cold temperatures within subvisible cirrus clouds observed during the Costa Rica Aura Validation Experiment in winter 2006. Results showed that they contained a few particles that were significantly larger (by about 100 μm) than the observations reported from the earlier measurements. Also, chemistry measurements suggested the presence of sulphates mixed with organics within these observed subvisible cirrus.

3.3. Cases Studies

3.3.1. Case Overview and Meteorological Context

[32] Many factors can affect the «Nic, IWC or R_{ei}-T or RH_{Ice}» relationships including nucleation type (homogeneous freezing, immersion/condensation freezing, contact freezing, deposition nucleation), processes of collision/aggregation and ice particle growth rates as well as vertical velocity. To better understand the physical processes explaining the differences between TIC-1/2A and TIC-2B, two ice clouds have been further investigated. The first one (TIC-1/2A F9) is characterized by a relatively small RH_{Ice} and made up of relatively high concentration of small ice crystals while the second one (TIC-2B F21) is characterized by a high RH_{Ice} and a low concentration of relatively large ice crystals. These two ice clouds have a vertical extent from 0 to ∼6.7 km height, temperature reaching low values below −30.0 ± 0.5°C and ice water content never exceeding 0.03 g m^{-3}. To better understand both types of ice clouds, the vertical variability of bulk and thermodynamic properties, the particle size distribution and the synoptic context in which they form are investigated. These two deep glaciated clouds were recorded on two spirals over the Barrow site; the flight F9 downdraft spiral on 1 April 2008 from 23:13:43 UTC to 23:45:43 UTC (Figure 5d), and the flight F21 updraft spiral on 15 April 2008 from 00:55:26 UTC to 01:17:23 UTC (Figure 6d).

[33] Figures 5 and 6 show the equivalent potential temperature with the mean sea level pressure (Figures 5a and 6a), the geopotential at 500 hPa (Figures 5b and 6b), the horizontal wind at 700 hPa (Figures 5c and 6c) and the

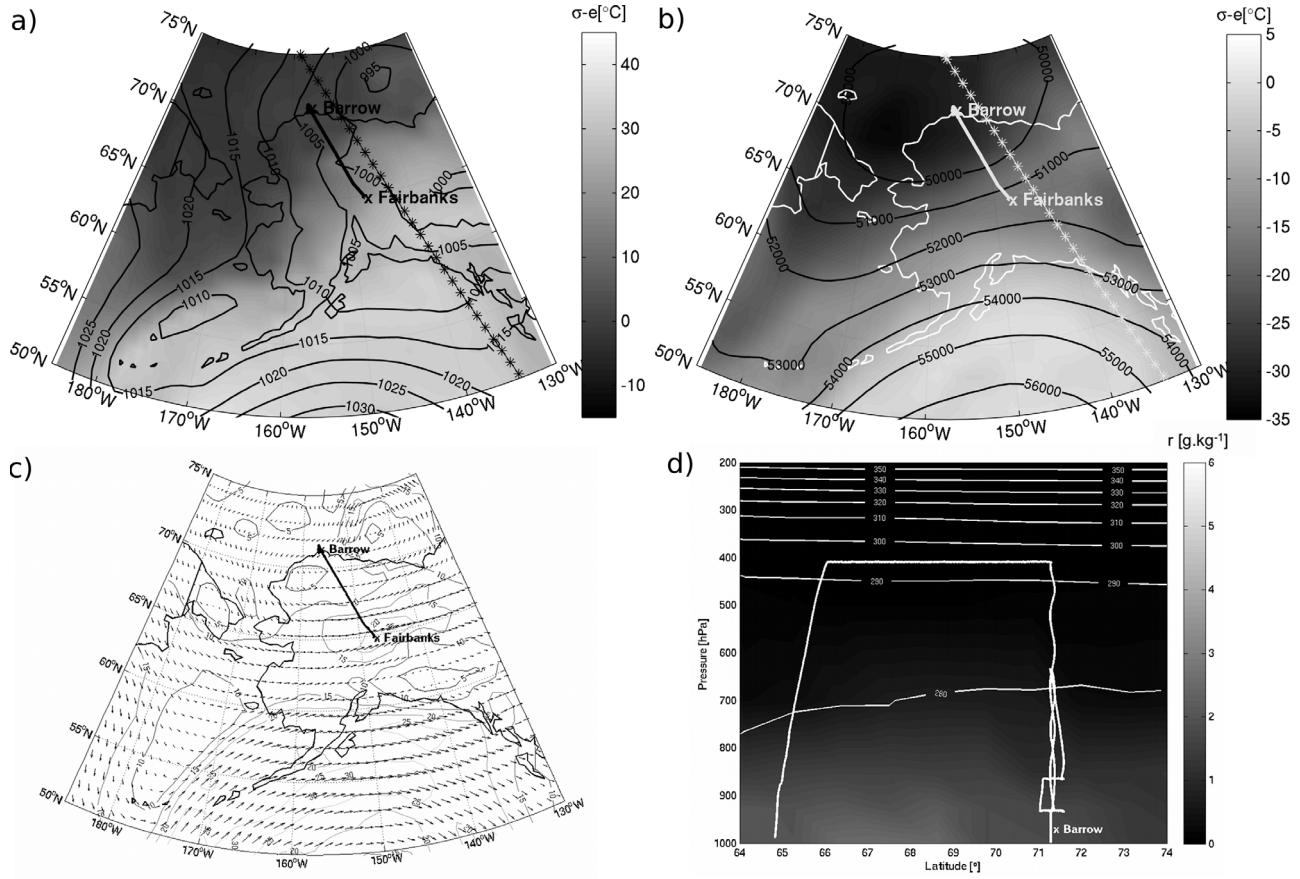

Figure 6. (a) Equivalent potential temperature (°C) with mean sea level pressure (hPa) and (b) geopotential (m^2 s^{-2}) at 500 hPa, (c) module and direction of horizontal wind at 700 hPa and (d) vertical profile of flight F21 (white solid line) with equivalent potential temperature (K) and mixing ratio (g kg^{-1}) over Alaska at 00:00:00 UTC (15 April 2008). A-Train overpass track (star line) is also shown at 2:06:30 UTC (14 April 2008).

vertical profile of flight trajectory (white) with the equivalent potential temperature and the mixing ratio (Figures 5d and 6d) over Alaska from the European Centre for Medium-range Weather Forecasts (ECMWF) operational analysis for both flights. On 1 April 2008 (F9), the polar jet stream moved across Alaska from the southwest to the northeast (Figure 5b). A low-pressure system, formed near Japan, follows a north-northeastward path toward Alaska before dissipating over the Bering Strait (Figure 5a). Winds at 700 hPa show a southerly flow over Alaska reaching ~10 m s^{-1} (Figure 5c) over Barrow. Vertical profiles of equivalent potential temperature and mixing ratio show that the F9 profile is in an area close to a warm front, characterized by theta-e contours almost vertical near the surface with a gradient gradually shifting to the west with height. The formation of cirrostratus in the F9 profile is therefore probably associated to the warm front.

[34] On 15 April 2008 (F21), the synoptic pattern is dominated by a decaying closed low-pressure system coming from the Chukchi Sea (Figures 6a and 6b), which dissipates over the NSA. The airborne measurements of spiral F21 over the Barrow site are made in the center of this decaying low-pressure system. The vertical profile of vertical velocity shows a weak subsiding vertical motion (figure not shown). The easterly winds are weak (~5 m s^{-1}) (Figure 6c) when compared to the F9 case study (1 April 2008). The equivalent potential temperature and mixing ratio do not vary much in the horizontal, which is characteristic of a homogeneous air mass (Figure 6d).

3.3.2. N_{Ti}-R_{ei}-RH_{Ice}-T_a Relationships

[35] Figure 7 shows the averaged particle size distribution measured by the 2DS in the size range 10–800 μm, the 2 DC in the size range 150–800 μm and the 2DP probes for diameters greater than 800 μm, for both ice clouds. In both cases, the ice crystal size distributions show a bimodal shape between 10 (lower limit imposed) to ~6500 μm with peaks at ~10–20 μm (1.36 L^{-1} μm^{-1}) and ~120 μm (0.084 L^{-1} μm^{-1}) for the F9 ice cloud and at ~10 μm (0.21 L^{-1} μm^{-1}) and ~315–415 μm (0.005 L^{-1} μm^{-1}) for the F21 ice cloud. The TIC-1/2A F9 has a larger concentration of ice particles smaller than 300 μm by a factor of 10 and a lower concentration of ice particles larger than 300 μm by a factor of 1.5 when compared to the TIC-2B F21. Similar concentrations for ice particles of diameter greater than 2000 μm are observed in both cases.

[36] Figure 8 summarizes Figures 4a, 4b, and 4d for both ice clouds F9 and F21. It shows the relative humidity with respect to ice as a function of air temperature measured in both ice clouds. Symbol size and color represent the number concentration and the effective radius of ice particles

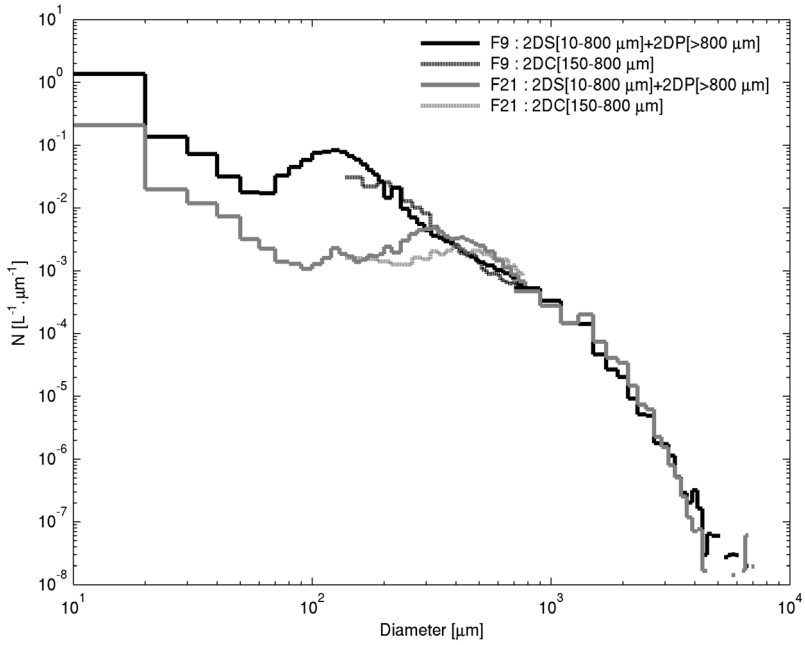

Figure 7. Averaged size distributions from 2DS, 2 DC and 2DP probes for F9 (1 April 2008) in the time interval 23:13:43–23:32:10 UTC (black line) and for F21 (15 April 2008) in the time interval 00:55:26–01:14:58 UTC (gray line).

respectively from the combination 2. Data values (RH_{Ice}, N_{ic}, R_{ei}) are averaged for each 2.5°C temperature interval. For both clouds, there is a clear tendency for RH_{Ice} to increase with increasing ice particle concentration and with decreasing air temperature and ice particle effective radius. This can be explained by the strength of the cooling rate, associated to synoptic scale conditions and the availability of ice nuclei. This is discussed further in section 4.

[37] The number concentration of ice particles in the TIC-2B F21 ice cloud is smaller with diameters larger when compared to the TIC-1/2A F9 ice cloud, while relative humidity over ice is larger in the TIC-2B F21 ice cloud.

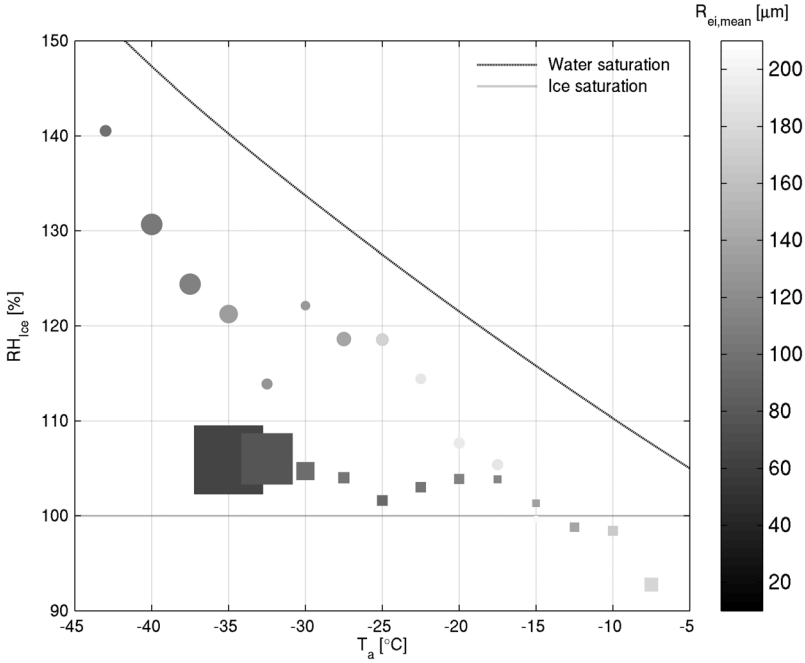

Figure 8. Relative humidity over ice as a function of temperature for ice clouds for flights F9 and F21. Data are averaged over each 30 s and 2.5°C interval. Symbol size represents $N_{ic,mean}$, and the bar color represents the $R_{ei,mean}$ of ice crystals from the combination 2 [2DS + 2DP].

Table 3. RH_{Ice}, N_{ic}, R_{ei} of Ice Clouds F9 and F21 Averaged Over Each 2.5°C Period of Air Temperature, With Their Associated Standard Deviation[a]

	F9			F21		
T_a (°C)	RH_{Ice} (%)	N_{ic} (L^{-1})	R_{ei} (μm)	RH_{Ice} (%)	N_{ic} (L^{-1})	R_{ei} (μm)
−42.5	-	-	-	140.5 ± 4.5	3.2 ± 4.2	99.8 ± 13.1
					2.7 ± 3.4	105.1 ± 22.9
−40	-	-	-	130.7 ± 5.3	10.7 ± 5.7	104.3 ± 9.3
					9.1 ± 4.8	112.2 ± 4.5
−37.5	-	-	-	124.4 ± 3.1	10.6 ± 2.3	111.8 ± 6.3
					9.3 ± 1.8	119.0 ± 5.5
−35	105.9 ± 2.3	180.7 ± 72.7	65.1 ± 7.6	121.3 ± 8.8	7.9 ± 2.4	132.8 ± 14.1
		188.1 ± 73.9	50.6 ± 5.1		7.3 ± 2.0	133.8 ± 10.2
−32.5	106.0 ± 0.8	100.2 ± 62.5	76.6 ± 6.0	113.9 ± 6.5	2.8 ± 1.7	127.2 ± 15.1
		101.7 ± 68.0	59.9 ± 5.4		2.6 ± 1.6	128.3 ± 13.2
−30	104.7 ± 2.3	12.4 ± 14.3	97.1 ± 14.5	122.1 ± 2.7	2.1 ± 1.2	130.1 ± 8.2
		10.8 ± 12.9	90.2 ± 20.7		2.0 ± 1.2	128.5 ± 8.4
−27.5	104.0 ± 2.2	4.86 ± 1.7	102.9 ± 6.4	118.6 ± 1.4	4.9 ± 1.0	140.7 ± 12.6
		4.2 ± 1.4	102.3 ± 4.5		4.6 ± 0.9	137.2 ± 12.9
−25	101.6 ± 3.2	4.2 ± 3.1	91.3 ± 6.1	118.6 ± 1.0	3.8 ± 1.0	173.1 ± 15.1
		3.6 ± 2.6	91.4 ± 5.5		3.9 ± 0.9	170.6 ± 15.5

[a]Values from the combination 2 (2DS + 2DP) and from the combination 1 (2DS + 2 DC + 2DP) are in black and gray, respectively.

Table 3 shows the three main parameters that define the main differences between the two types of ice clouds investigated: the averaged ice concentration, the averaged ice effective radius and the averaged relative humidity over ice from instrument combination 2 (in black) and 1 (in gray) with the associated standard deviation. Differences between instrument combinations 1 and 2 are small when compared to differences between both cases for a given variable and a given instrument combination. Table 3 also shows that the differences of N_{ic}, RH_{Ice} and R_{ei} between both clouds increase as the temperature decreases. This suggests that differences should be the largest at cloud top where the temperature is the coldest.

3.3.3. Vertical Variability of Cloud Properties

3.3.3.1. The 1 April 2008 F9 Ice Cloud

[38] A low-level mixed phase cloud extended from near the surface to ~2 km height as shown by the temperature inversion (see Figure 9a). This mixed phase cloud is characterized by a very large concentration greater than 10^3 L^{-1} μm^{-1} of liquid droplets smaller than 30 μm

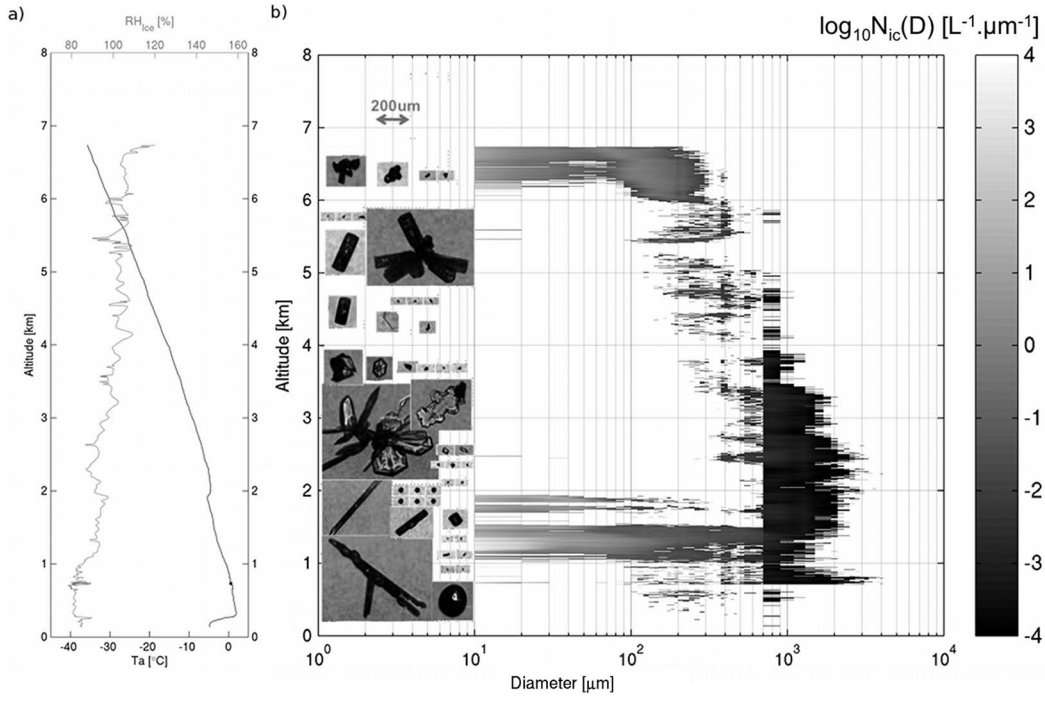

Figure 9. (a) Air temperature from the reverse-flow probe and relative humidity over ice from the EG&G chilled mirror hygrometer. (b) N(D) (L^{-1} μm^{-1}) as a function of ice crystal diameter (μm) from 2DS (10–800 μm) and 2DP (>800 μm observed during F9). CPI images above show representative crystal shape and size to the corresponding altitude for the profile of F9 (1 April 2008) for the time interval 23:13:43–23:45:43 UTC.

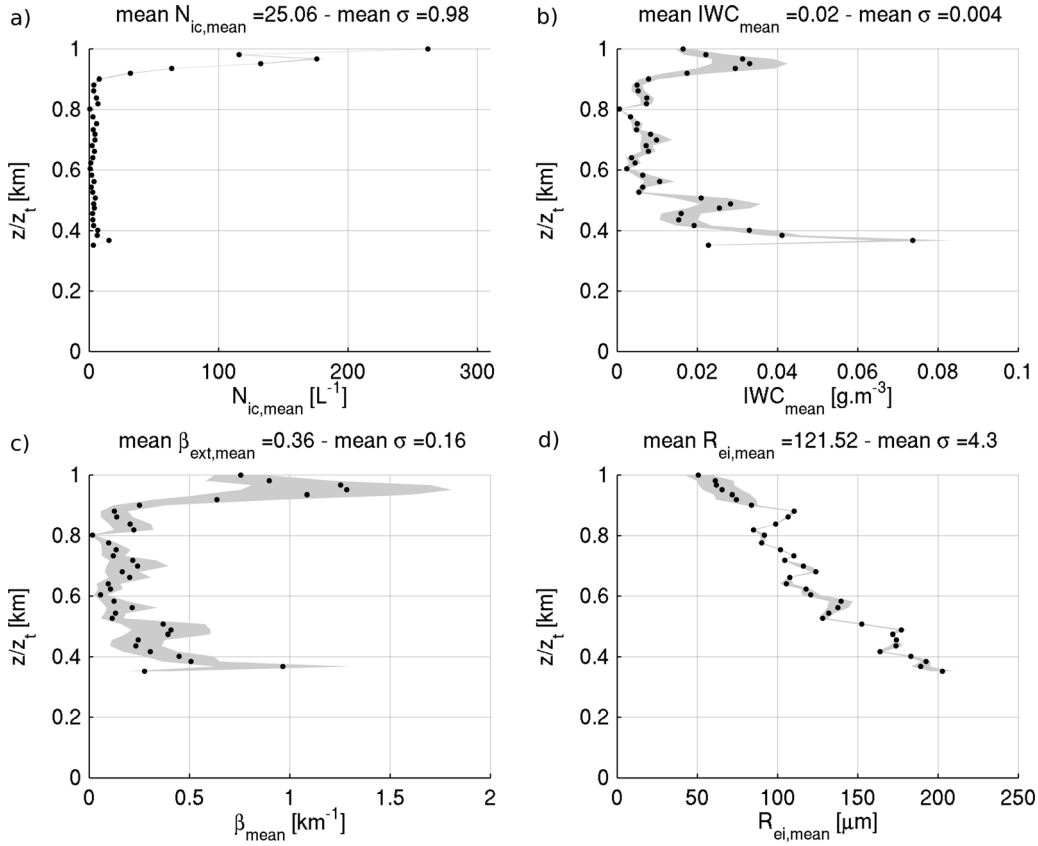

Figure 10. Averaged N_{ic}, IWC, β_{ext} and R_{ei} between combinations 1 and 2 in the Figure 3 caption with their associated standard deviation as a function of normalized height for the ice cloud F9 (1 April 2008). Data are averaged over each 30 s period. Z_t in Table 2 was used to normalize the values.

(Figure 9b). The reported maximum relative humidity over water (RH_{Water}) in the mixed phase cloud below 2 km altitude is 92.3% (never exceeds 100%) at $T_a = -5°C$ (see Figure 9). According to *Lin and Hubbard* [2004] the uncertainty should be around ±6%. Therefore RH_{Ice} values should have been biased quite a bit low in this case. Above this mixed phase layer, the F9 deep ice cloud extends up to an altitude of 6.7 km. It is characterized by a relatively large number concentration of particles smaller than 200 μm in diameter at the top. Figure 9 shows that N_{ic} and derived bulk parameters IWC and β_{ext} peak to values of 261.6 L^{-1}, 0.03 g m^{-3} and 1.28 km^{-1}, respectively. CPI images show that most of the particles were quasi-spheroidal, compact assemblages of plates, faceted polycrystals and irregulars becoming larger downward. Ice particles shape within F9 ice cloud seems to match with ice particles shape collecting in midlatitude winter storm to define both mass-diameter (equation (2)) and mass-area (equation (1)) relationships discussed above [*Mitchell et al.*, 1990]. However, the M90 database is composed of rimed habits, that the CPI probe does not seem to have measured within F9 ice cloud. Ice particles start to nucleate on ice nuclei when the relative humidity with respect to ice (RH_{Ice}) is larger than 100%. RH_{Ice} exceeded 100% above 4 km where the temperature is −16.0°C and reaches 120.1% at cloud top where the temperature is −35.7°C. The layer between 4 km and cloud top is therefore the region where ice crystals nucleate. This can also be seen by the concentration of small particles, which increases from 4 km to the cloud top. This is consistent with the classical theory of ice nucleation by deposition in which the nucleation rate increases as the ice supersaturation increases [*Pruppacher and Klett*, 1997]. The response of the RID probe throughout the F9 ice cloud indicates that there was no trace of supercooled water. This is consistent with the relatively low values of RH_{Ice} (Figure 8) closed to the ice saturation. These conditions suggest that the dominant nucleation process could be deposition ice nucleation.

[39] Below 6 km, the ice crystal number concentration, ice water content and extinction coefficient rapidly decrease. They remain approximately constant afterward with values of ∼4 L^{-1}, ∼0.01 g m^{-3} and ∼0.24 km^{-1} respectively down to the mixed phase cloud top. The ice crystal effective radius gradually increases from ∼50 μm at cloud top to ∼202 μm above the mixed phase cloud top (Figure 10). The drop in ice crystal number concentration and ice water content below 6 km seems to be related to the entrainment of drier air between 4 and 6 km coming from the south that can be seen on satellite images (CALIPSO lidar and CloudSat radar) in Figure 11 at 71.3°N latitude. The sublimation of ice particles in such an environment could contribute to decrease the ice water content substantially. Since the sublimation rate is inversely proportional to the ice crystal dimension, small ice crystals quickly sublimate thus contributing to increase the ice crystal effective radius. The sublimation can also affect the ice crystal habits and make

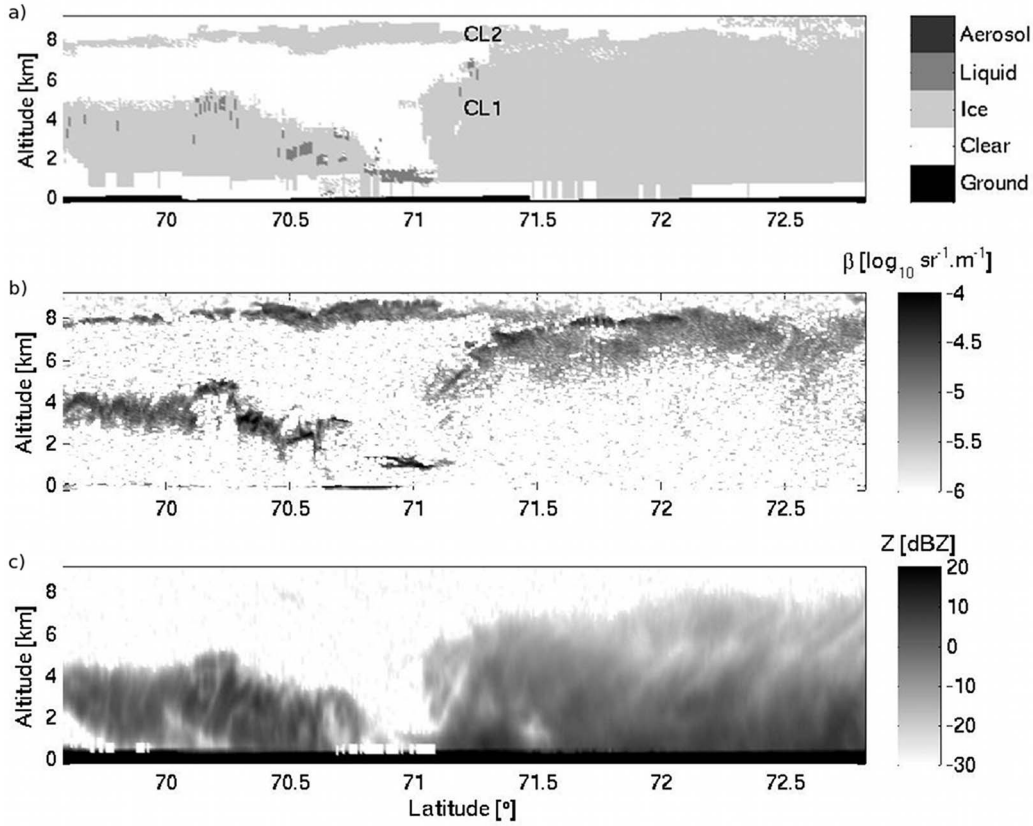

Figure 11. TIC1/2A observed on 1 April 2008: (a) Dardar Mask, (b) total lidar attenuated backscatter and (c) radar reflectivity.

the collision/aggregation processes more efficient. *Korolev and Isaac* [2004] presented images of sublimated particles resulting in smooth surface features, rounded corners and disappearing facets. These images were in perfect agreement with sublimating ice particles and aggregates (irregular particles) observed by the CPI probe in the cloud layer between 4 and 6 km (Figure 9b).

[40] The F9 ice cloud was also sampled by CloudSat and CALIPSO satellites. The distance between the aircraft and satellite projected tracks was about ~70 km over Barrow. The time lap between the aircraft track and the satellite overpass varied between ~30 min at 23:13:43 UTC to ~1 h at 23:45:43 UTC. Observation time and location are different and therefore in situ and satellite measurements are not sampling the same scene. Yet, ice clouds observed by in situ and satellites are part of the same low-pressure system and not too far from each other in time and space. The objective is to see whether the DARDAR synergistic radar-lidar products can differentiate the TIC-1/2A and TIC-2B and reproduce the vertical structure of these ice clouds and thus confirm the in situ measurements. Figures 11 and 12 show key input parameters of CALIOP, CloudSat, and the DARDAR synergistic radar-lidar products derived from CloudSat and CALIPSO measurements. On 1 April 2008, radar and lidar measurements (see Figures 10a, 10b, and 10c) indicate two ice cloud layers around the Barrow site (~71.3°N). A first layer extended from the surface to ~6–7 km (hereafter CL1) and a second thin ice cloud (hereafter CL2) at ~8.6 km (Figure 11a). No in situ measurements were made in CL2; it is therefore ignored in this analysis. Few precipitating ice crystals are seen by the radar between the surface and 4 km. Figure 11a exhibits a merged mask created using both radar and lidar measurements following *Delanoë and Hogan* [2010]. In this very cold region, most of the cloud was glaciated but one can notice supercooled layers at 5–7 km altitude at 71.2°N latitude identified using the strong lidar return of CALIOP. This is not in agreement with the RID probe that shows no supercooled water in the F9 ice cloud. Given the fact that the air was subsaturated with respect to liquid water and that the RID probe has not detected any liquid water, it is very likely that the supercooled liquid layer is in fact a DARDAR algorithm artifact probably due to the noisy daytime lidar signal. According to the AWAC4 algorithm for the TICs classification of *Grenier et al.* [2009], this glaciated cloud is defined as a TIC-1/2A (figure not shown) and there is no liquid supercooled layer.

[41] Figure 12 shows the vertical profiles of the DARDAR retrieved properties (IWC, β_{ext}, and R_e) on different latitude slices around the Barrow site. The satellite observation is an instantaneous picture of the cloud and since the airborne sampling time is considerably longer, the cloud microstructure may have changed. It implies that we cannot directly compare profile-to-profile in situ and satellites measurements [*Delanoë et al.*, 2012]. For this reason, different latitude slices are used to get a better representation of the flight in situ measurements. In the upper first km of the cloud (i.e., between 0.7 to 1 (normalized height)), between 71.0 and 71.5°N latitude, IWC ranges from 0.001 to 0.035 g m^{-3}, β_{ext}

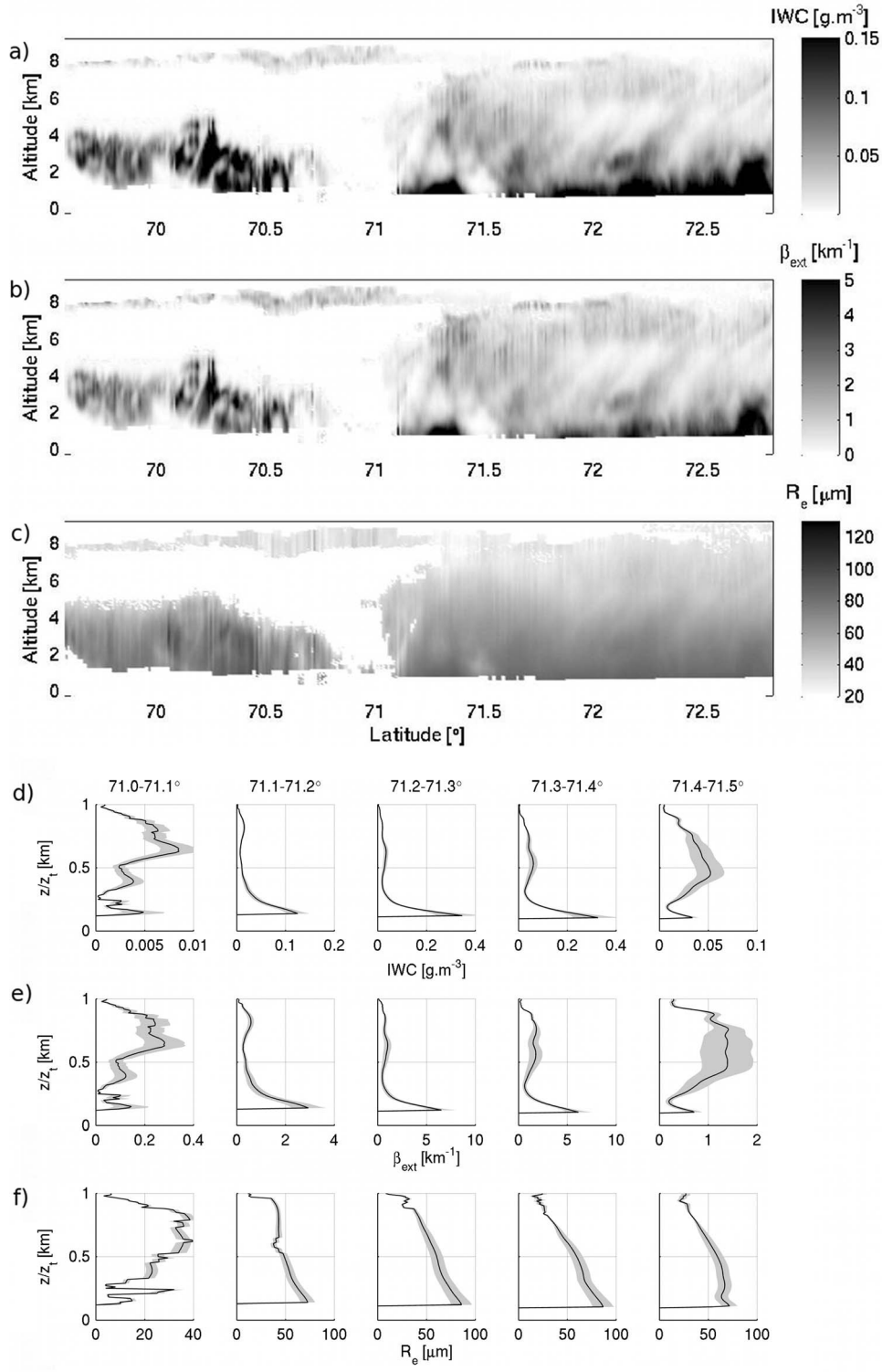

Figure 12. Latitude-height representation of the synergistic CloudSat radar and CALIPSO lidar retrieval of ice cloud properties: (a, d) ice water content, (b, e) visible extinction and (c, f) effective radius for the 1 April 2008 case.

from 0.02 to 1.82 km^{-1} and R_e from 3.24 to 48.51 μm. This is in agreement with in situ measurements for IWC and β_{ext} in terms of order of magnitude in the upper part of the ice cloud. The ice effective radius is very sensitive to the assumption made on the mass-diameter relationship and its definition. Therefore, these results should be rather viewed as the relative differences between the two case studies since absolute values of bulk quantities are highly uncertain.

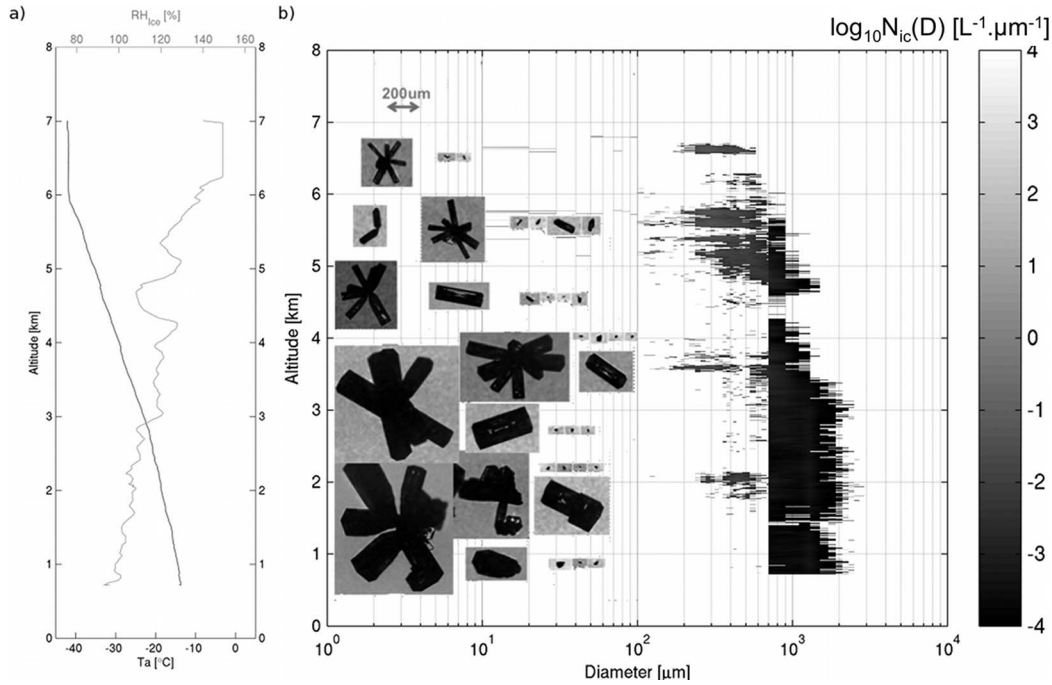

Figure 13. (a) Air temperature from the reverse-flow probe and relative humidity over ice from the EG&G chilled mirror hygrometer and (b) N(D) (L^{-1} μm^{-1}) as a function of ice crystal diameter (μm) from 2DS (10–800 μm) and 2DP (>800 μm) during observed F21. CPI images above show representative crystal shape and size to the corresponding altitude for the profile of F21 (15 April 2008) for the time interval 00:55:26–01:17:24 UTC.

3.3.3.2. The 15 April 2008 F21 Ice Cloud

[42] Figure 13 shows a cloud layer extending from near the surface to a height of approximately 6.7 km. The ice crystal size distribution suggests that the deep cloud layer was mostly composed of large precipitating ice particles (mainly from 200 to 3000 μm diameter) with a very low number concentration (<5 L^{-1} on average) (Figure 13b). Cloud air temperature varies from about −14.0°C at the surface down to −42.2°C at the cloud top. RH_{Ice} was relatively large and reached values up to 149.4% at the top of the cloud (Figure 13a). At cloud top, there is a sharp increase of N_{ic}, IWC and R_{ei} up to 14.2 L^{-1}, 0.02 g m^{-3} and 100 μm, respectively, within a relatively thin layer. The increase of these bulk quantities for the ice cloud observed on 1 April was slower. Then, a substantial drop in N_{ic}, IWC and β_{ext} at ∼4.3 km (i.e., at ∼0.6 (normalized height)) is observed except for R_{ei}, which slightly decreases. Below this height, the IWC remains approximately constant while N_{ic} decreases to less than 5 L^{-1} and remains almost constant while R_{ei} increases from ∼120 μm to 211 μm (Figure 14). The drop of N_{ic} and IWC could be related either to the entrainment of drier air at this height or to the lack of 2DP data (seen on the Figure 13b at 4.3 km height).

[43] The response of the RID probe throughout the F21 ice cloud indicates that trace amount of supercooled water was present and the CPI images do not show the presence of sublimating ice particles. This is consistent with the RH_{Ice} vertical profile, which shows values close to the saturation with respect to liquid water.

[44] Figure 13b shows that pristine rosettes, columns and bullet rosettes are the dominant crystal habit through the cloud. *Bailey and Hallett* [2004, 2009] found that "pristine rosettes" (i.e., rosette shapes that are not mixed habit and are without plate like and side-plane features) only form at temperatures below −40°C and that columns and bullet rosettes are frequent at colder temperatures (T < −40°C) with ice supersaturation around 25%. The ice cloud F21 is associated to a cold decaying low-pressure system, which is characterized by a weak downward vertical motion (figure not shown). In this environment, air parcels can stay long periods of time in quasi-equilibrium between deposition and production of ice supersaturation due to a slow cooling of the air mass by infrared radiation. In these conditions of very low temperature and high ice supersaturation, ice crystals may have time to reach an equilibrium state for the development of normal hexagonal and rectangular faces by depositional freezing as shown by the images of perfect forms of rosette bullets seen by the CPI probe.

[45] CloudSat and CALIPSO did not sample the F21 ice cloud on 15 April 2008. However, there was an overpass about 3 h before at about 170 km to the east of the sampling profile (Figure 6). The synoptic patterns were very similar on 14 April and 15 April with the presence of the same decaying low-pressure system moving slowly from the Arctic Ocean with an easterly flow, i.e., toward the Barrow site. The synoptic pattern and thermodynamic structure of the atmosphere (Figure 6) are very similar to the time of the F21 flight. Moreover, the Millimeter Cloud Radar based at Barrow shows the presence of the extended deep ice cloud between 03:00 UTC 14 April 2008 to 15:00 UTC 15 April 2008 (figure not shown). It is therefore reasonable to assume

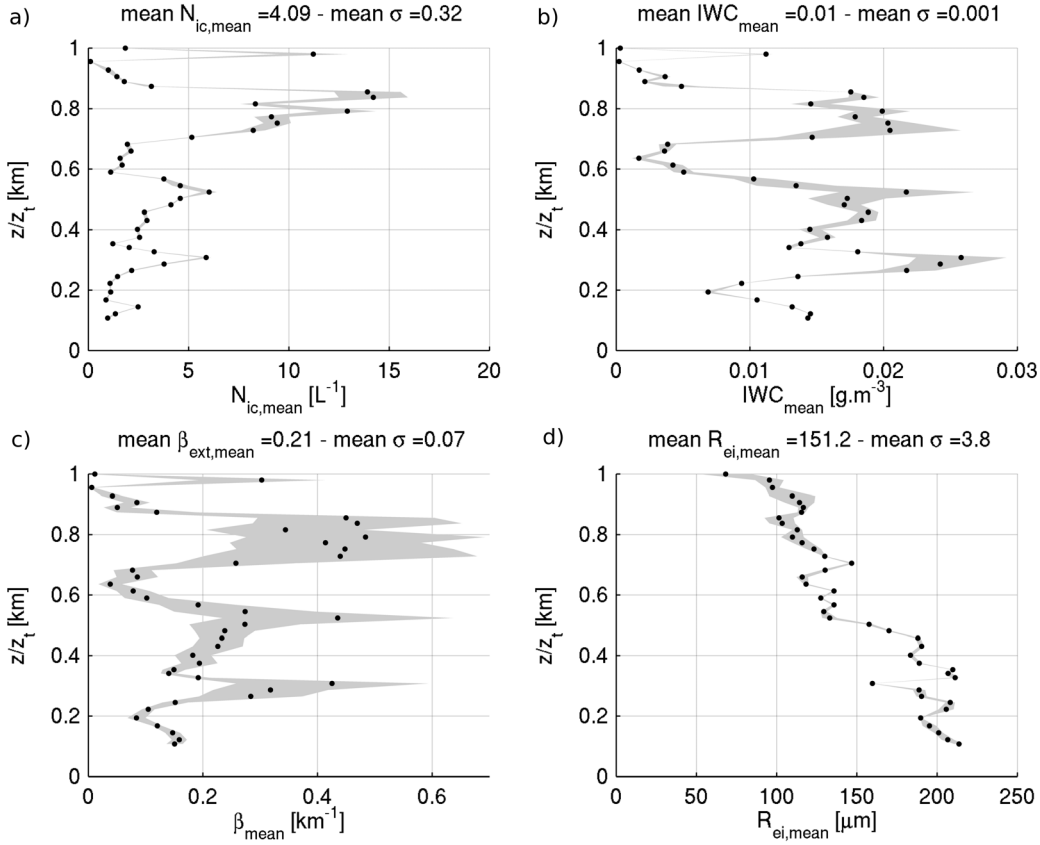

Figure 14. Averaged N_{ti}, IWC, β_{ext} and R_{ei} between combinations 1 and 2 in the Figure 3 caption with their associated standard deviation as a function of normalized height for the ice cloud F21 (15 April 2008). Data are averaged over each 30 s period. Z_t in Table 2 was used to normalize the values.

that the cloud microstructure was not very different than 3 h later.

[46] At the time of the satellite overpass, radar and lidar measurements suggest the superposition of two layers of air with the presence of a cloud-free area identified by CALIPSO from 70°N to 72°N latitudes (Figure 15). Both cloud layers extended from the surface up to ~5.2 and ~5.7 km at 71.0°N and 71.5°N respectively. Larger values of radar reflectivity (Figure 15c) and lidar depolarization ratio (figure not shown) support the presence of precipitating nonspherical ice crystals in the deep glaciated cloud, consistent with the CPI images. Figure 15a shows that most of the cloud was glaciated. However, several traces of supercooled water were dispersed through the cloud. This is in agreement with the response of the RID probe indicating that supercooled water was present. Further, it is noted that traces of liquid water observed in this cloud are not likely to be cloud water droplets but rather haze droplets. Some traces of aerosol are also visible just above the cloud at 69.5 to 70°N latitude at 4 km height. According to the AWAC4 algorithm for the TICs classification of *Grenier et al.* [2009], this deep ice cloud is defined as a TIC-2B (figure not shown).

[47] Figure 16 shows the vertical profiles of retrieved properties on different longitude slices around the Barrow site. In the first km, at the top of the cloud between 0.7 to 1 (normalized height), IWC varies from 0.001 to 0.021 g m^{-3}, β_{ext} from 0.061 to 0.65 km^{-1} and R_e from 15.90 to 53.83 μm. These results agree well with in situ measurements (Figure 10) for IWC and β_{ext} at cloud top in terms of order of magnitude.

[48] Table 4 shows the averaged values of β, Z and R_e retrieved from the Varcloud algorithm as a function of the normalized altitude between the latitude 71.0–71.5°N, for the F9 and F21 ice clouds. The averaged R_e of the TIC-2B F21 ice cloud is greater by a factor of ~1.3 (compared to ~1.7 for airborne data) on the first 2 km at the top when compared to the averaged R_e of the TIC-1/2A F9 ice cloud. This results in a R_e vertical profile steeper for the TIC-2B F21 ice cloud, i.e., an explosive growth of the ice crystals by water vapor diffusion. In the TIC-1/2A F9 case, the ice crystal growth is more progressive and slow.

[49] These two case studies (TIC-1/2A F9 and TIC-2B F21) have similar cloud top height, optical depth, temperature and ice water content. Yet, the vertical profile of the number concentration and size of ice crystals are very different. The relative humidity with respect to ice is also higher in the TIC-2B F21 ice cloud almost reaching the saturation with respect to liquid water. Furthermore, traces of liquid water were also observed in the TIC-2B F21 ice cloud. These differences occur mainly in the upper part of both clouds where ice crystals nucleate.

[50] The IN concentration is possibly determinant for these clouds. Indeed, a large concentration of IN allows increasing N_{ic} and lowering the ice supersaturation.

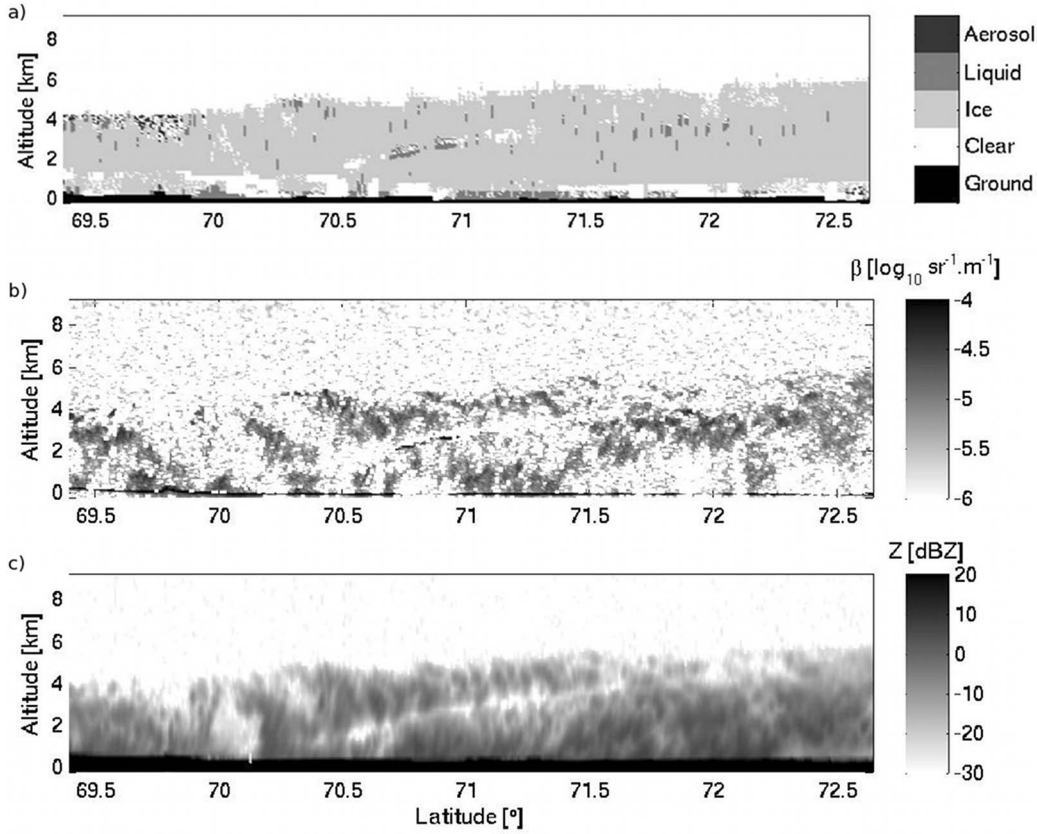

Figure 15. TIC2 observed on 14 April 2008: (a) Dardar Mask, (b) total lidar attenuated backscatter and (c) radar reflectivity.

Unfortunately, the CFDC was not functional during the flight F9. It is therefore not possible to make a direct comparison between the flights F9 and F21. However, other TIC-1/2A and TIC-2B selected cases (see Table 2) provide some information on the IN concentration. There are flights F20, F21 (TICs-2B) and F29 (TIC-1/2A). Figure 17 shows the average IN concentration from the CFDC probe, measured in range of $-11°C$ to $-42°C$ T_a and 0–40% RH_{Ice}, throughout the flights F20, F21 and F29. No CFDC IN concentration data were available at the time interval of the F29 ice cloud defined in Table 2. However, it is assumed that the average IN concentration measured over the entire flight from Barrow to Fairbanks is representative of the ice cloud air masses identified in Table 2. This assumption is based on the comparison of the average IN concentration inside TIC-2B F20 and F21 (selected ice clouds in Table 2) to the average IN concentration of the entire flights F20 and F21 and similar IN concentration values in range of 1 to 5 L^{-1}. Obviously IN concentration between two locations spaced more than 800 km could differ a lot, as IN concentration measured nearer-surface compared to the higher elevations. These results should be considered preliminary estimates. Results shows that the IN concentration is larger for flight F29 (2 orders of magnitude) when compared to flights F20 and F21. This is consistent with the large (small) ice crystal concentration of flights F29 (F20 and F21). These results suggest that the IN concentration was probably larger in the TIC-1/2A F9 ice cloud when compared to the TIC-2B F21 ice cloud.

[51] In the TIC-1/2A F9 ice cloud, a relatively large IN concentration allows for the nucleation of ice crystals by water vapor deposition at lower saturation with respect to ice, i.e., where ice nucleation is efficient. At cloud top, there is no input of precipitating ice crystals. Also, the air mass cools radiatively during the slow TIC life cycle. Therefore, the relative humidity with respect to ice cannot decrease without the contribution of ice nucleation by deposition. The relatively large ice crystal concentration combined to the moderate ice supersaturation lead to the growth of ice crystals by water vapor deposition and aggregation at a relatively small rate. This is shown by the gradual increase of the ice crystal effective radius from the cloud top to lower cloud levels.

[52] In the case of the TIC-2B F21 case, the IN concentration is very low. Consequently, the ice crystal concentration remains low allowing for the ice supersaturation to increase up to values near saturation with respect to liquid water. Traces of liquid water observed in this cloud are not likely to be cloud water droplets since the air is slightly undersaturated with respect to liquid water. They could be rather produced by haze droplets, which can be detected by the spaceborne CALIPSO lidar [*van Diedenhoven et al.*, 2011]. In condition close to liquid water saturation, soluble aerosols could grow to sizes relatively large. Consequently, these haze droplets become diluted enough and freeze by either immersion or condensation freezing. But these processes typically occur at higher ice supersaturation than the

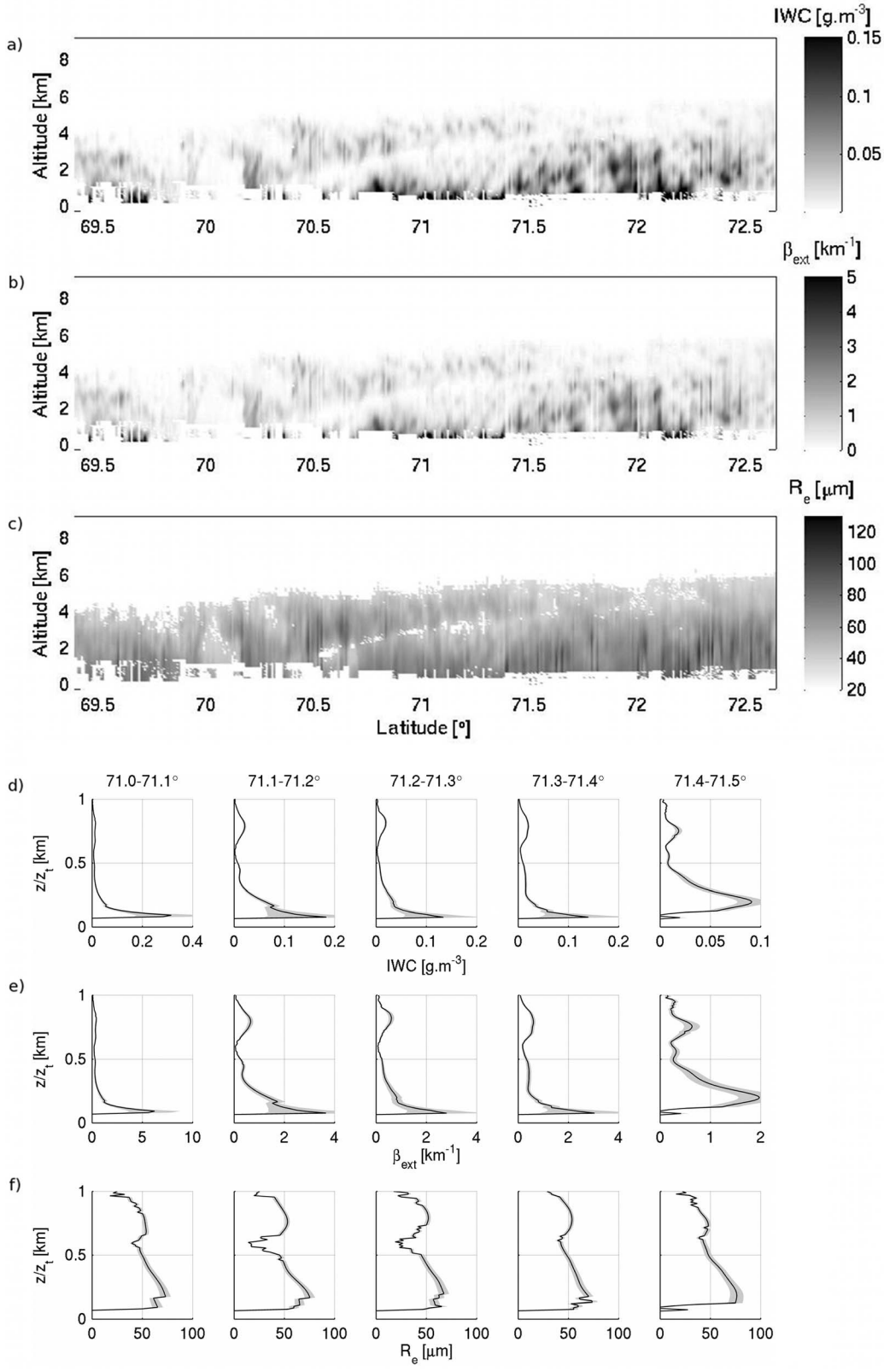

Figure 16. Latitude-height representation of the synergistic CloudSat radar and CALIPSO lidar retrieval of ice cloud properties: (a, d) ice water content, (b, e) visible extinction and (c, f) effective radius for the 14 April 2008 case.

Table 4. The β, Z and R_e From Varcloud Algorithm of Ice Clouds F9 and F21 Averaged Between 71.0°N to 71.5°N With Their Associated Standard Deviation, According to the Normalized Altitude

	F9 Zt_{mean} = 7600 m			F21 Zt_{mean} = 5940 m		
z/z_t	β ($\log_{10}$ sr^{-1} m^{-1})	**Z** (dBZ)	R_e (μm)	β ($\log_{10}$ sr^{-1} m^{-1})	**Z** (dBz)	R_e (μm)
[1–0.9]	−5.31 ± 0.20	−30.0 ± 2.3	27.6 ± 1.2	−5.69 ± 0.11	−30.0 ± 2.0	36.8 ± 1.0
[0.9–0.8]	−5.25 ± 0.09	−22.7 ± 1.9	33.6 ± 2.5	−5.59 ± 0.10	−21.6 ± 3.5	41.7 ± 2.4
[0.8–0.7]	−5.45 ± 0.06	−16.7 ± 2.0	40.7 ± 2.2	−5.31 ± 0.09	−12.8 ± 1.8	49.4 ± 2.0
[0.7–0.6]	−5.45 ± 0.05	−12.2 ± 1.2	46.6 ± 1.9	−5.46 ± 0.14	−14.0 ± 2.3	49.4 ± 1.8
[0.6–0.5]	−5.62 ± 0.10	−9.8 ± 0.3	52.3 ± 1.9	−5.60 ± 0.06	−20.2 ± 1.1	45.5 ± 0.5
[0.5–0.4]	−5.71 ± 0.08	−9.2 ± 0.1	57.2 ± 1.1	−5.55 ± 0.08	−15.7 ± 2.5	48.8 ± 2.6
[0.4–0.3]	−5.77 ± 0.07	−8.5 ± 0.5	60.8 ± 1.4	−5.49 ± 0.05	−10.1 ± 1.6	57.0 ± 2.9
[0.3–0.2]	−5.80 ± 0.08	−7.7 ± 0.8	65.9 ± 2.2	−5.36 ± 0.11	−4.4 ± 1.9	66.4 ± 3.0
[0.2–0.1]	−5.65 ± 0.19	−1.7 ± 3.2	71.8 ± 6.0	−5.17 ± 0.06	0.5 ± 1.8	73.5 ± 1.6
[0.1–0]	−5.78 ± 0.07	20.7 ± 13.7	0.0 ± 0.0	−5.07 ± 0.40	23.3 ± 13.6	79.3 ± 3.1

onset ice supersaturation for deposition nucleation reported in this case [e.g., *Eastwood et al.*, 2009]. Low concentration of IN in the deposition mode combined to the high ice supersaturated air lead to an explosive growth of ice crystals by water vapor diffusion. This can be seen by the sharp R_{ei} gradient at the top of the TIC-2B F21 ice cloud. As a result, the F21 cloud is composed essentially of a relatively low concentration of precipitating ice crystals whereas the TIC-1/2A F9 ice cloud is composed by a top layer of small ice crystals in relatively large number concentrations, which gradually grow to precipitating sizes by water vapor diffusion and collision processes.

4. Discussion

[53] Recent laboratory experiments have shown that good ice nuclei such as kaolinite particles can be "deactivated" when they are coated with various chemical species such as ammonium sulphate, ammonium bisulphate, sulfuric acid and some organics [e.g., *Eastwood et al.*, 2009; *Chernoff and Bertram*, 2010]. These experiments have shown that the onset ice supersaturation at which ice nucleation occurs (in the immersion mode) is substantially increased close to the liquid saturation point when the kaolinite particles are coated with sulfuric acid compared to uncoated particles (in the deposition mode). According to *Sullivan et al.* [2010], the IN deactivation effect of sulphuric acid on dust particle is irreversible and still active once the acid has been neutralized with ammonia.

[54] *Grenier et al.* [2009] hypothesized that clouds composed of a small concentration of large precipitating ice crystals (TIC-2B) observed with CloudSat and CALIPSO over the Arctic during winter could also be linked to acid coating on IN concentration in polluted air masses. Modeling studies using box models, single-column models and regional climate models evaluating the impact of the IN deactivation effect by acid coating on the cloud microstructure, precipitation and radiation have also been performed over the last 10 years [*Girard and Blanchet*, 2001; *Girard et al.*, 2005, 2012; *Girard and Stefanof*, 2007]. All these modeling investigations have shown that acid coating on IN leads to fewer but larger ice crystals in ice clouds at cold temperatures. These previous modeling studies have also shown that the ice supersaturation is larger in TIC-2B clouds when compared to TIC-1/2A clouds. Therefore, satellite, in situ and laboratory observations, and modeling studies concur to support the hypothesis that these clouds (TIC-2B) are linked to aerosols composition, possibly with a highly acidic coating dominant in the Arctic during the cold season [*Sirois and Barrie*, 1999] whereas TIC-1/2A clouds would form in a more pristine environment [*Grenier et al.*, 2009]. Results presented in this paper also suggest that TIC-2B form in air masses containing relatively low IN concentrations whereas TIC-1/2A form in air masses with larger IN concentration. Because of the small number of cases investigated and the limited availability of the CFDC during ISDAC, the link between the IN concentration and the type of TIC will need to be further investigated in future campaigns.

[55] A recent study on the large-scale transport of aerosols to Alaska during April 2008 was performed by *Atkinson et al.* [2011]. Results were based on synoptic meteorological analysis, air mass back trajectory studies using the Lagrangian Particle Dispersion Model (FLEXPART) and on the lidar, surface lidar and balloon-borne aerosol measurements at the

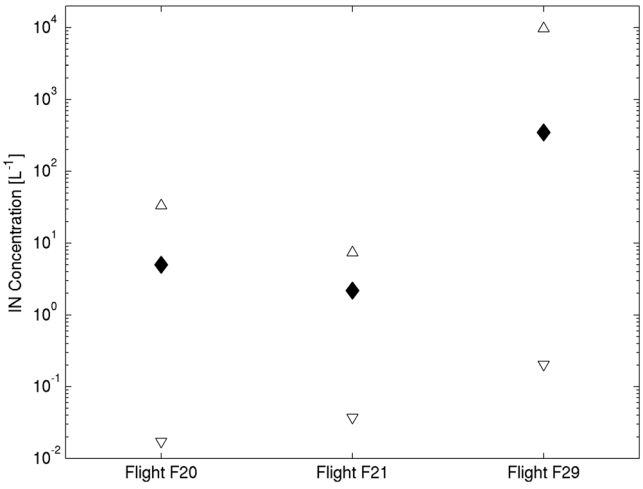

Figure 17. Average ice nuclei concentrations from the CFDC probe measured in range of −11°C to −42°C and 0–40% supersaturation with respect to ice (solid diamonds) with upper limit (open triangles) and lower limit (open inverse triangles) throughout flights F20 (106 values), F21 (57 values), and F29 (44 values). During periods in which the CFDC was sampling outside these conditions, NaN (not a number) was used as a placeholder in the data set.

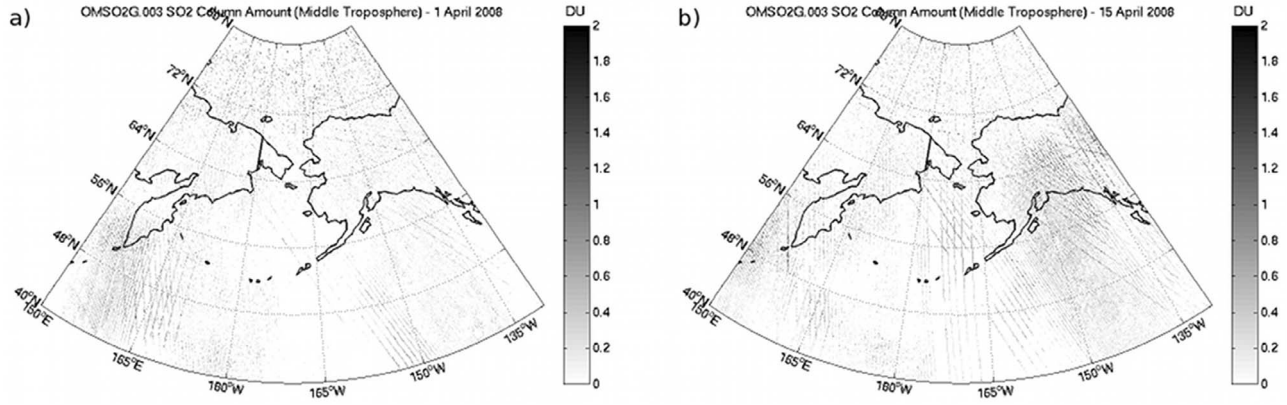

Figure 18. Satellite measurements of SO_2 total columns by OMI on (a) 1 April 2008 and (b) 15 April 2008.

Fairbanks site. Results show that Alaska experienced several major aerosol-loading events in April 2008. The first few days of April (1 April to midday 5 April 2008) were dominated by pristine clear conditions with a very low aerosol concentration. This is in agreement with the PCASP measurements that were performed during flights F9, F11 and F12 (see Table 2). Satellite observations have also shown pristine conditions on a wider scale south of Fairbanks. This appears to result from the presence of a low-pressure system located to the west of Alaska leading to an atmospheric flow into the Alaska Interior from the western North Pacific Ocean. *Atkinson et al.* [2011] suggest a combination of several factors and processes that contributed to greatly reduce the aerosol loading such as the lost of aerosols during transport by wet deposition/precipitation processes associated to a long residence time over the Pacific Ocean and forced topographic ascent. The second week of April (midday 5 to 17 April 2008) was dominated by Asian dust with some smoke probably resulting from a flow from northern China and southeastern Siberia, maintained by the presence of an anticyclone in the central North Pacific. As opposed to the pristine period, the air mass quickly crosses the ocean and has not passed over the Alaska Range. Smoke comes from biomass burning in the Kazakhstan and southern Siberia regions [*Warneke et al.*, 2009]. Moreover dust aerosols come possibly from the Gobi (28 March 2008) and Takla Makan (2 April 2008) dust-raising events, which would have reached the Alaska Interior given the favorable large-scale circulation patterns. However, *Burton et al.* [2011], who made several flights in the Fairbanks-Barrow area during the same period of spring during ARCTAS (Arctic Research of the Composition of the Troposphere from Aircraft and Satellites), reported a small occurrence of dust but large occurrence of haze and smoke.

[56] These studies suggest that the TIC-1/2A F9 (1 April 2008) formed in a pristine environment, whereas the TIC-2B F21 (15 April 2008) appears to have been formed in a more polluted environment composed of Asian dust with smoke. This is also supported by satellite observations of SO_2 concentration over the NSA from the Ozone Monitoring Instrument (OMI) (see Figure 18) showing that the SO_2 concentration, precursor of sulfuric acid, was higher on 15 April 2008 than on 1 April 2008 over Alaska. These observations confirm *Atkinson et al.*'s [2011] results and indicate that the aerosols on 15 April were likely to be moderately to highly acidic. It is likely that aerosols have been acidified during their transport by the large amount of SO_2. Yet a direct link between acidic aerosols and TIC-2B clouds remains to be established.

5. Summary and Conclusion

[57] The objectives of this study were to characterize the microphysical and thermodynamical properties of TIC-1/2A and TIC-2B clouds using airborne measurements taken during the ISDAC campaign conducted over the NSA during April 2008. A statistical study was performed on a set of ISDAC cloud profiles, associated to different types of ice clouds (TICs). This was done in order to determine the relationships between RH_{Ice}, T_a, N_{ic}, IWC, R_{ei} for each type of ice cloud (TIC-1/2A and TIC-2B). From this study, two types of ice clouds have been distinguished. The first type (TIC-1/2A) is composed by a large concentration of small ice crystals whereas the second type (TIC-2B) is composed of a smaller concentration of larger and precipitating ice crystals. The relative humidity with respect to ice is larger in the second type of ice cloud when compared to the first type. Two ice clouds representing each type were investigated in greater details. They are the ice cloud cases observed on 1 April 2008 (TIC-1/2A F9) and on 15 April 2008 (TIC-2B F21). Both have similar vertical extent, temperature and ice water content. Results show that most of the differences between the two clouds are located near cloud top where the nucleation of ice crystals occurs. In the TIC-2B F21 case, few ice crystals nucleate at high ice supersaturation and grow very rapidly to precipitating sizes. In the TIC-1/2A cloud, a larger number of ice crystals nucleate and they grow at a slower pace by water vapor diffusion and aggregation to precipitating sizes.

[58] A possible explanation for these differences between both cloud types is the availability of active IN at relatively low ice supersaturation. Recent modeling and observational studies combined to the results presented in this study support the SIFI hypothesis, that is acidic coating on IN could explain the formation of TIC-2B at the expense of TIC-1/2A. Moreover, satellite observations (e.g., MODIS, CALIPSO, OMI) and back trajectory analysis of *Atkinson et al.* [2011] also support this hypothesis.

[59] Further investigations will be needed to confirm a link between TIC-2B clouds and acidic aerosols. The ice nuclei and acidic information of aerosols are needed to make a better assessment on IN nucleation capability. Volcanic emissions provide a source of sulfate throughout the troposphere that is not neutralized by natural ammonia emission, thus keeping a higher degree of acidity. Volcanoes are therefore interesting to study the link between highly acidic aerosols and TIC-2B. In April 2008, sustained eruptive and noneruptive (continuous degassing) activity was recorded at Karymsky and Shiveluck volcanoes in Kamchatka peninsula; Cleveland and Veniaminof volcanoes in the Aleutian Islands, i.e., regions that several air masses cross before reaching the Alaska Interior. Future work will be needed to link air masses influenced by these active volcanoes and the ice cloud formation during ISDAC.

[60] **Acknowledgments.** This work was funded by the Natural Sciences and Engineering Research Council of Canada (NSERC), the Fonds Québécois de la Recherche sur la Nature et la Technologie (FQRNT) and the Centre National d'Etudes Spatiales (CNES). ISDAC was supported by the U.S. Department of Energy (DOE) Atmospheric Radiation Measurement (ARM) Program Climate Research Facility, the DOE Atmospheric Sciences Program, the National Research Council of Canada, and Environment Canada. ISDAC data were obtained from the ARM program archive, sponsored by the U.S. DOE, Office of Science, Office of Biological and Environmental Research, Environmental Sciences Division. We thank the ICARE Data and Services Center (http://www.icare.univ-lille1.fr/) for providing access to the spaceborne data used in this study. The ECMWF is acknowledged for the access to the forecasts and analysis used in this study. Valuable suggestions for ice crystal instrumental analysis of Greg McFarquhar, Paul Lawson and Qixu Mo were appreciated.

References

Atkinson, D. E., K. Sassen, M. Hayashi, C. F. Cahill, G. Shaw, D. Harrigan, and H. Fuelberg (2011), ARCTAS-A ground-based observational campaign and meteorological context, interior Alaska, April 2008, *Atmos. Chem. Phys. Discuss.*, *11*, 16,499–16,552, doi:10.5194/acpd-11-16499-2011.

Bailey, M. P., and J. Hallett (2004), Growth rates and habits of ice crystals between −20° and −70°C, *J. Atmos. Sci.*, *61*, 514–554, doi:10.1175/1520-0469(2004)061<0514:GRAHOI>2.0.CO;2.

Bailey, M. P., and J. Hallett (2009), A comprehensive habit diagram for atmospheric ice crystals: Confirmation from the laboratory, AIRS II, and other field studies, *J. Atmos. Sci.*, *66*, 2888–2899, doi:10.1175/2009JAS2883.1.

Baker, B. A., and R. P. Lawson (2006a), In situ observations of the microphysical properties of wave, cirrus, and anvil clouds. Part I: Wave clouds, *J. Atmos. Sci.*, *63*, 3160–3185, doi:10.1175/JAS3802.1.

Baker, B. A., and R. P. Lawson (2006b), Improvement in determination of ice water content from two-dimensional particle imagery. Part I: Image-to-mass relationships, *J. Appl. Meteorol. Climatol.*, *45*, 1282–1290, doi:10.1175/JAM2398.1.

Barrie, L. A., and M. J. Barrie (1990), Chemical components of lower tropospheric aerosols in the high Arctic: Six years of observations, *J. Atmos. Chem.*, *11*(3), 211–226, doi:10.1007/BF00118349.

Bigg, E. K. (1980), Comparison of aerosol at four baseline atmospheric monitoring stations, *J. Appl. Meteorol.*, *19*, 521–533, doi:10.1175/1520-0450(1980)019<0521:COAAFB>2.0.CO;2.

Blanchet, J.-P., and E. Girard (1994), Arctic 'greenhouse cooling', *Nature*, *371*, 383, doi:10.1038/371383a0.

Brown, P. R. A., and P. N. Francis (1995), Improved measurements of the ice water content in cirrus using a total-water probe, *J. Atmos. Oceanic Technol.*, *12*, 410–414, doi:10.1175/1520-0426(1995)012<0410:IMOTIW>2.0.CO;2.

Burton, S. P., R. A. Ferrare, C. A. Hostetler, J. W. Hair, R. R. Rogers, M. D. Obland, C. F. Butler, A. L. Cook, D. B. Harper, and K. D. Froyd (2011), Aerosol classification using airborne High Spectral Resolution Lidar measurements—Methodology and examples, *Atmos. Meas. Tech. Discuss.*, *4*, 5631–5688, doi:10.5194/amtd-4-5631-2011.

Campbell, J. R., D. L. Hlavka, E. J. Welton, C. J. Flynn, D. D. Turner, J. D. Spinhirne, V. S. Scott and I. H. Hwang (2002), Full-time eye-safe cloud and aerosol lidar observations at Atmospheric Radiation Measurement Program sites: Instruments and data processing. *J. Atmos. Oceanic Technol.*, *19*(4), 431–442, doi:10.1175/1520-0426(2002)019<0431:FTESCA>2.0.CO;2.

Chernoff, D. I., and A. K. Bertram (2010), Effects of sulfate coatings on the ice nucleation properties of a biological ice nucleus and several types of minerals, *J. Geophys. Res.*, *115*, D20205, doi:10.1029/2010JD014254.

Cober, S. G., G. A. Isaac, and A. V. Korolev (2001), Assessing the Rosemount icing detector with in situ measurements. *J. Atmos. Oceanic Technol.*, *18*(4), 515–528, doi:10.1175/1520-0426(2001)018<0515:ATRIDW>2.0.CO;2.

Delanoë, J., and R. J. Hogan (2008), A variational scheme for retrieving ice cloud properties from combined radar, lidar and infrared radiometer, *J. Geophys. Res.*, *113*, D07204, doi:10.1029/2007JD009000.

Delanoë, J., and R. J. Hogan (2010), Combined CloudSat-CALIPSO-MODIS retrievals of the properties of ice clouds, *J. Geophys. Res.*, *115*, D00H29, doi:10.1029/2009JD012346.

Delanoë, J., A. Protat, O. Jourdan, J. Pelon, M. Papazzoni, R. Dupuy, J. F. Gayet, and C. Jouan (2012), Comparison of airborne in-situ, airborne radar-lidar, and spaceborne radar-lidar retrievals of polar ice cloud properties sampled during the POLARCAT campaign, *J. Atmos. Oceanic Technol.*, doi:10.1175/JTECH-D-11-00200.1, in press.

Dufresne, J.-L., and S. Bony (2008), An assessment of the primary sources of spread of global warming estimates from coupled atmosphere-ocean models, *J. Clim.*, *21*, 5135–5144, doi:10.1175/2008JCLI2239.1.

Eastwood, M. L., S. Cremel, M. Wheeler, B. J. Murray, E. Girard, and A. K. Bertram (2009), Effects of sulfuric acid and ammonium sulfate coatings on the ice nucleation properties of kaolinite particles, *Geophys. Res. Lett.*, *36*, L02811, doi:10.1029/2008GL035997.

Field, P. R., A. J. Heymsfield, and A. Bansemer (2006), Shattering and particle interarrival times measured by optical array probes in ice clouds, *J. Atmos. Oceanic Technol.*, *23*, 1357–1371, doi:10.1175/JTECH1922.1.

Foot, J. S. (1988), Some observations of the optical properties of clouds II: Cirrus, *Q. J. R. Meteorol. Soc.*, *114*, 145–164, doi:10.1002/qj.49711447908.

Gayet, J.-F., F. Auriol, A. Minikin, J. Ström, M. Seifert, R. Krejci, A. Petzol, G. Febvre, and U. Schuman (2002), Quantitative measurement of the microphysical and optical properties of cirrus clouds with four different in situ probes: Evidence of small crystals, *Geophys. Res. Lett.*, *29*(24), 2230, doi:10.1029/2001GL014342.

Girard, E., and J. P. Blanchet (2001), Simulation of Arctic diamond dust and ice fog or thin stratus using an explicit aerosol-cloud-radiation model, *J. Atmos. Sci.*, *58*, 1199–1221, doi:10.1175/1520-0469(2001)058<1199:SOADDI>2.0.CO;2.

Girard, E., and A. Stefanof (2007), Assessment of the dehydration-greenhouse feedback over the Arctic during February 1990, *Int. J. Climatol.*, *27*, 1047–1058, doi:10.1002/joc.1455.

Girard, E., J.-P. Blanchet, and Y. Dubois (2005), Effects of sulphuric acid aerosols on wintertime low-level atmospheric ice crystals, humidity, and temperature at Alert, Nunavut, *Atmos. Res.*, *73*, 131–148, doi:10.1016/j.atmosres.2004.08.002.

Girard, E., G. Dueymes, P. Du, and A. K. Bertram (2012), Assessment of the effects of acid-coated ice nuclei on the Arctic cloud microstructure, atmospheric dehydration, radiation and temperature during winter, *Int. J. Climatol.*, doi:10.1002/joc.3454, in press.

Grenier, P., and J. P. Blanchet (2010), Investigation of the sulphate-induced freezing inhibition effect from CloudSat and CALIPSO measurements, *J. Geophys. Res.*, *115*, D22205, doi:10.1029/2010JD013905.

Grenier, P., J. P. Blanchet, and R. Munoz-Alpizar (2009), Study of polar thin ice clouds and aerosols seen by CloudSat and CALIPSO during mid-winter 2007, *J. Geophys. Res.*, *114*, D09201, doi:10.1029/2008JD010927.

Gultepe, I., and D. O. Starr (1995), A comparison of evaporative cooling with infrared heating beneath a cirrus cloud, *Atmos. Res.*, *35*, 217–231, doi:10.1016/0169-8095(94)00020-E.

Gultepe, I., G. A. Isaac, and S. G. Cober (2001), Ice crystal number concentration versus temperature for climate studies, *Int. J. Climatol.*, *21*, 1281–1302, doi:10.1002/joc.642.

Hassol, S. J. (2005), *Impacts of a Warming Arctic: Arctic Climate Impact Assessment*, Cambridge Univ. Press, Cambridge, U. K.

Heymsfield, A. J., S. Lewis, A. Bansemer, J. Iaquinta, L. M. Miloshevich, M. Kajikawa, C. Twohy, and M. R. Poellot (2002), A general approach for deriving the properties of cirrus and stratiform ice cloud particles, *J. Atmos. Sci.*, *59*, 3–29, doi:10.1175/1520-0469(2002)059<0003:AGAFDT>2.0.CO;2.

Hirdman, D., J. F. Burkhart, H. Sodemann, S. Eckhardt, A. Jefferson, P. K. Quinn, S. Sharma, J. Ström, and A. Stohl (2010), Long-term trends of black carbon and sulphate aerosol in the Arctic: Changes in atmospheric transport and source region emissions, *Atmos. Chem. Phys. Discuss.*, *10*, 12,133–12,184, doi:10.5194/acpd-10-12133-2010.

Intergovernmental Panel on Climate Change (2007), *Climate Change 2007: The Physical Science Basis: Working Group I Contribution to the Fourth*

Assessment Report of the IPCC, edited by S. Solomon et al., Cambridge Univ. Press, New York.

Intrieri, J. M., and M. D. Shupe (2004), Characterization and radiative effects of diamond dust of the Western Arctic Ocean region, *J. Clim.*, *17*, 2953–2960, doi:10.1175/1520-0442(2004)017<2953:CAREOD>2.0.CO;2.

Intrieri, J. M., C. W. Fairall, M. D. Shupe, P. O. G. Persson, E. L. Andreas, P. Guest, and R. M. Moritz (2002), An annual cycle of Arctic surface cloud forcing at SHEBA, *J. Geophys. Res.*, *107*(C10), 8039, doi:10.1029/2000JC000439.

Jensen, E. J., et al. (2009), On the importance of small ice crystals in tropical anvil cirrus, *Atmos. Chem. Phys.*, *9*, 5519–5537, doi:10.5194/acp-9-5519-2009.

King, W. D., D. A. Parkin, and R. J. Handsworth (1978), A hot-wire liquid water device having fully calculable response characteristics, *J. Appl. Meteorol.*, *17*, 1809–1813, doi:10.1175/1520-0450(1978)017<1809:AHWLWD>2.0.CO;2.

Korolev, A. V., and G. A. Isaac (2004), Observation of sublimating ice particles in clouds, paper presented at 14th International Conference on Clouds and Precipitation, Int. Comm. on Clouds and Precip., Bologna, Italy.

Korolev, A. V., and G. A. Isaac (2006), Relative humidity in liquid, mixed-phase, and ice clouds, *J. Atmos. Sci.*, *63*, 2865–2880, doi:10.1175/JAS3784.1.

Korolev, A. V., and I. P. Mazin (2003), Supersaturation of water vapor in clouds, *J. Atmos. Sci.*, *60*, 2957–2974, doi:10.1175/1520-0469(2003)060<2957:SOWVIC>2.0.CO;2.

Korolev, A. V., J. W. Strapp, and G. A. Isaac (1998), Evaluation of the accuracy of PMS optical array probes, *J. Atmos. Oceanic Technol.*, *15*, 708–720, doi:10.1175/1520-0426(1998)015<0708:EOTAOP>2.0.CO;2.

Korolev, A. V., E. F. Emery, J. W. Strapp, S. G. Cober, G. A. Isaac, M. Wasey, and D. Marcotte (2011), Small ice particles in tropospheric clouds: Fact or artifact? Airborne Icing Instrumentation Evaluation Experiment, *Bull. Am. Meteorol. Soc.*, *92*, 967–973, doi:10.1175/2010BAMS3141.1.

Krämer, M., et al. (2009), Ice supersaturations and cirrus cloud crystal numbers, *Atmos. Chem. Phys.*, *9*, 3505–3522, doi:10.5194/acp-9-3505-2009.

Lampert, A., A. Ehrlich, A. Dörnbrack, O. Jourdan, J. F. Gayet, G. Mioche, V. Shcherbakov, C. Ritter, and M. Wendisch (2009), Microphysical and radiative characterization of a subvisible midlevel Arctic ice cloud by airborne observations—A case study, *Atmos. Chem. Phys.*, *9*, 2647–2661, doi:10.5194/acp-9-2647-2009.

Lance, S., C. A. Brock, D. Rogers, and J. A. Gordon (2010), Water droplet calibration of the Cloud Droplet Probe (CDP) and in-flight performance in liquid, ice and mixed-phase clouds during ARCPAC, *Atmos. Meas. Tech.*, *3*, 1683–1706, doi:10.5194/amt-3-1683-2010.

Law, K. S., and A. Stohl (2007), Arctic air pollution: Origins and impacts, *Science*, *315*, 1537–1540, doi:10.1126/science.1137695.

Lawson, R. P. (2011), Effects of ice particles shattering on the 2D-S probe, *Atmos. Meas. Tech.*, *4*, 1361–1381, doi:10.5194/amt-4-1361-2011.

Lawson, R. P., B. A. Baker, C. G. Schmitt, and T. L. Jensen (2001), An overview of microphysical properties of Arctic clouds observed in May and July 1998 during FIRE ACE, *J. Geophys. Res.*, *106*, 14,989–15,014, doi:10.1029/2000JD900789.

Lawson, R. P., D. O'Connor, P. Zmarzly, K. Weaver, B. Baker, Q. Mo, and H. Jonsson (2006a), The 2D-S (Stereo) Probe: Design and preliminary tests of a new airborne, high-speed, high-resolution particle imaging probe, *J. Atmos. Oceanic Technol.*, *23*, 1462–1477, doi:10.1175/JTECH1927.1.

Lawson, R. P., B. Baker, B. Pilson, and Q. Mo (2006b), In situ observations of the microphysical properties of wave, cirrus, and anvil clouds, Part II: Cirrus clouds, *J. Atmos. Sci.*, *63*, 3186–3203, doi:10.1175/JAS3803.1.

Lawson, R. P., B. Pilson, B. Baker, Q. Mo, E. Jensen, L. Pfister, and P. Bui (2008), Aircraft measurements of microphysical properties of subvisible cirrus in the tropical tropopause layer, *Atmos. Chem. Phys.*, *8*, 1609–1620, doi:10.5194/acp-8-1609-2008.

Lin, X., and K. G. Hubbard (2004), Uncertainties of derived dewpoint temperature and relative humidity, *J. Appl. Meteorol.*, *43*, 821–825, doi:10.1175/2100.1.

Mazin, I. P., A. V. Korolev, A. Heymsfield, G. A. Isaac, and S. G. Cober (2001), Thermodynamics of icing cylinder for measurements of liquid water content in supercooled clouds, *J. Atmos. Oceanic Technol.*, *18*, 543–558, doi:10.1175/1520-0426(2001)018<0543:TOICFM>2.0.CO;2.

McFarquhar, G. M., J. Um, M. Freer, D. Baumgardner, G. L. Kok, and G. Mace (2007), Importance of small ice crystals to cirrus properties: Observations from the Tropical Warm Pool International Cloud Experiment (TWP-ICE), *Geophys. Res. Lett.*, *34*, L13803, doi:10.1029/2007GL029865.

McFarquhar, G. M., et al. (2011), The indirect and semi-direct aerosol campaign, *Bull. Am. Meteorol. Soc.*, *92*, 183–201, doi:10.1175/2010BAMS2935.1.

Mitchell, D. L., R. Zhang, and R. L. Pitter (1990), Mass-dimensional relationships for ice particles and the influence of riming on snowfall rates, *J. Appl. Meteorol.*, *29*, 153–163, doi:10.1175/1520-0450(1990)029<0153:MDRFIP>2.0.CO;2.

Moran, K. P., B. E. Martner, M. J. Post, R. A. Kropfli, D. C. Welsh, and K. G. Widener (1998), An unattended cloud-profiling radar for use in climate research, *Bull. Am. Meteorol. Soc.*, *79*, 443–455, doi:10.1175/1520-0477(1998)079<0443:AUCPRF>2.0.CO;2.

Morrison, H., K. D. Curry, M. D. Shupe, and P. Zuidema (2005), A new double-moment microphysics parameterization for application in cloud and climate models. Part II: Single-column modeling of arctic clouds, *J. Atmos. Sci.*, *62*, 1678–1693, doi:10.1175/JAS3447.1.

Morrison, H., G. de Boer, G. Feingold, J. Harrington, M. D. Shupe, and K. Sulia (2011), Resilience of persistent Arctic mixed-phase clouds, *Nat. Geosci.*, *5*, 11–17, doi:10.1038/ngeo1332.

Protat, A., G. M. McFarquhar, J. Um, and J. Delanoë (2011), Obtaining best estimates for the microphysical and radiative properties of tropical ice clouds from TWP-ICE in situ microphysical observations, *J. Appl. Meteorol. Clim.*, *50*, 895–915, doi:10.1175/2010JAMC2401.1.

Pruppacher, H. R., and J. D. Klett (1997), *Microphysics of Clouds and Precipitation*, 2nd ed., Kluwer Acad., Dordrecht, Netherlands.

Quinn, P. K., G. Shaw, E. Andrews, E. G. Dutton, T. Ruoho-Airola, and S. L. Gong (2007), Arctic haze: Current trends and knowledge gaps, *Tellus, Ser. B*, *59*, 99–114, doi:10.1111/j.1600-0889.2006.00238.x.

Sassen, K., and B. S. Cho (1992), Subvisual-thin cirrus lidar dataset for satellite verification and climatological research, *J. Appl. Meteorol.*, *31*, 1275–1285, doi:10.1175/1520-0450(1992)031<1275:STCLDF>2.0.CO;2.

Sassen, K., J. M. Comstock, Z. Wang, and G. Mace (2001), Cloud and aerosol research capabilities at FARS: The Facility for Atmospheric Remote Sensing, *Bull. Am. Meteorol. Soc.*, *82*, 1119–1138, doi:10.1175/1520-0477(2001)082<1119:CAARCA>2.3.CO;2.

Shupe, M. D. (2011), Clouds at Arctic atmospheric observatories, Part II: Thermodynamic phase characteristics, *J. Appl. Meteorol. Climatol.*, *50*, 645–661, doi:10.1175/2010JAMC2468.1.

Shupe, M. D., and J. M. Intrieri (2004), Cloud radiative forcing of the Arctic surface: The influence of cloud properties, surface albedo, and solar zenith angle, *J. Clim.*, *17*, 616–628, doi:10.1175/1520-0442(2004)017<0616:CRFOTA>2.0.CO;2.

Shupe, M. D., V. P. Walden, E. Eloranta, T. Uttal, J. R. Campbell, S. M. Starkweather, and M. Shiobara (2011), Clouds at Arctic atmospheric observatories, Part I: Occurrence and macrophysical properties, *J. Appl. Meteorol. Climatol.*, *50*, 626–644, doi:10.1175/2010JAMC2467.1.

Sirois, A., and L. A. Barrie (1999), Arctic lower tropospheric aerosol trends and composition at Alert, Canada: 1980–1995, *J. Geophys. Res.*, *104*, 11,599–11,618, doi:10.1029/1999JD900077.

Sullivan, R. C., et al. (2010), Irreversible loss of ice nucleation active sites in mineral dust particles caused by sulphuric acid condensation, *Atmos. Chem. Phys.*, *10*, 11,471–11,487, doi:10.5194/acp-10-11471-2010.

van Diedenhoven, B., A. M. Fridlind, and A. S. Ackerman (2011), Influence of humidified aerosol on lidar depolarization measurements below ice-precipitating Arctic stratus, *J. Appl. Meteorol. Climatol.*, *50*, 2184–2192, doi:10.1175/JAMC-D-11-037.1.

Warneke, C., et al. (2009), Biomass burning in Siberia and Kazakhstan as the main source for Arctic haze over the Alaskan Arctic in April 2008, *Geophys. Res. Lett.*, *36*, L02813, doi:10.1029/2008GL036194.

Zelenyuk, A., D. Imre, M. Earle, R. Easter, A. Korolev, R. Leaitch, P. Liu, A. M. Macdonald, M. Ovchinnikov, and W. Strapp (2010), In situ characterization of cloud condensation nuclei, interstitial, and background particles using the Single Particle Mass Spectrometer, SPLAT II, *Anal. Chem.*, *82*, 7943–7951, doi:10.1021/ac1013892.